Mon. Not. R. Astron. Soc. **340,** 1317–1345 (2003)

Empirical calibration of the near-infrared Ca II triplet – IV. The stellar population synthesis models

A. Vazdekis,[1⋆] A. J. Cenarro,[2] J. Gorgas,[2] N. Cardiel[2,3] and R. F. Peletier[4]

[1]*Instituto de Astrofísica de Canarias, Vía Láctea s/n, La Laguna 38200, Tenerife, Spain*
[2]*Department de Astrofísica, Fac. de Ciencias Físicas, Universidad Complutense de Madrid, 28040 Madrid, Spain*
[3]*Calar Alto Observatory, CAHA, Apdo 511, 04004, Almería, Spain*
[4]*School of Physics and Astronomy, University of Nottingham, University Park, Nottingham NG7 2RD*

Accepted 2003 January 6. Received 2002 October 16

ABSTRACT

We present a new evolutionary stellar population synthesis model, which predicts spectral energy distributions for single-age single-metallicity stellar populations (SSPs) at resolution 1.5 Å (FWHM) in the spectral region of the near-infrared Ca II triplet feature. The main ingredient of the model is a new extensive empirical stellar spectral library that has been recently presented by Cenarro et al., which is composed of more than 600 stars with an unprecedented coverage of the stellar atmospheric parameters.

Two main products of interest for stellar population analysis are presented. The first is a spectral library for SSPs with metallicities $-1.7 < [Fe/H] < +0.2$, a large range of ages (0.1–18 Gyr) and initial mass function (IMF) types. They are well suited to modelling galaxy data, since the SSP spectra, with flux-calibrated response curves, can be smoothed to the resolution of the observational data, taking into account the internal velocity dispersion of the galaxy, allowing the user to analyse the observed spectrum in its own system. We also produce integrated absorption-line indices (namely CaT*, CaT and PaT) for the same SSPs in the form of equivalent widths.

We find the following behaviour for the Ca II triplet feature in old-aged SSPs: (i) the strength of the CaT* index does not change much with time for all metallicities for ages larger than ∼3 Gyr; (ii) this index shows a strong dependence on metallicity for values below $[M/H] \sim -0.5$; and (iii) for larger metallicities this feature does not show a significant dependence either on age or on the metallicity, being more sensitive to changes in the slope of power-like IMF shapes.

The SSP spectra have been calibrated with measurements for globular clusters by Armandroff & Zinn, which are well reproduced, probing the validity of using the integrated Ca II triplet feature for determining the metallicities of these systems. Fitting the models to two early-type galaxies of different luminosities (NGC 4478 and 4365), we find that the Ca II triplet measurements cannot be fitted unless a very dwarf-dominated IMF is imposed, or if the Ca abundance is even lower than the Fe abundance. More details can be found in work by Cenarro et al.

Key words: stars: fundamental parameters – globular clusters: general – galaxies: abundances – galaxies: elliptical and lenticular, cD – galaxies: evolution – galaxies: stellar content.

1 INTRODUCTION

This is the fourth and final paper in a series devoted to understanding the behaviour of the near-infrared Ca II triplet feature in stars and in stellar populations. The ultimate aim of this work is to use the strength of the Ca II triplet lines in this spectral range to investigate the stellar content of early-type galaxies, but the results are sufficiently general to be used in other areas (starburst and active galaxies, globular clusters or stellar astrophysics) as well. In Cenarro et al. (2001a) (hereafter Paper I) we presented a new empirical stellar spectral library, mostly observed at the 1-m Jacobus Kapteyn Telescope (JKT) at the Observatorio del Roque de Los Muchachos,

⋆E-mail: vazdekis@ll.iac.es

La Palma. The library is composed of 706 stars covering the Ca II triplet feature in the near-infrared. In that paper we provided a new index definition for this feature (CaT*) that, among other advantages, minimizes the effects of the Paschen series. For the stars in this library we derived a set of homogeneous atmospheric parameters in Cenarro et al. (2001b) (hereafter Paper II). In Cenarro et al. (2002) (hereafter Paper III) we described the behaviour of the Ca II triplet through empirical fitting functions, which relate the strength of this feature to the stellar atmospheric parameters. In the current paper, we make use of these functions and the spectra of the stellar library to predict both the strength of the Ca II triplet feature and spectral energy distributions (SEDs) in the range λλ8348.85–8950.65 for single-age, single-metallicity stellar populations (SSPs) by means of evolutionary stellar population synthesis modelling.

Traditionally, elliptical galaxies have been thought to be a uniform class of objects, with global properties changing smoothly with mass and hosting old and coeval stellar population. However, over the last decade, a growing body of evidence is indicating that the formation processes and star formation histories of, at least, an important fraction of early-type galaxies are more complex and heterogeneous. The apparent age spread among elliptical galaxies (González 1993; Faber et al. 1995; Jørgensen 1999), the distribution of element abundances (Worthey 1998; Peletier 1999; Trager et al. 2000a) and the interpretation of the scaling relations (such as the colour–magnitude or Mg_2–σ relations (Bower, Lucey & Ellis 1992; Bender, Burstein & Faber 1993; Colless et al. 1999; Terlevich et al. 1999; Kuntschner 2000, hereafter K00; Trager et al. 2000b, hereafter T00; Proctor & Sansom 2002, hereafter PS02), are some of the main issues in the present debate concerning the evolutionary status of early-type galaxies. These studies have been possible thanks to the comparison of observed data with the predictions of the, so-called, stellar population synthesis models. These models make use of a theoretical isochrone, or Hertzsprung–Russell diagram, convert isochrone parameters to observed ones, assuming empirical or theoretical prescriptions, and finally integrate along the isochrone assuming an initial mass function (IMF) (e.g. Tinsley 1980; Bruzual 1983; Arimoto & Yoshii 1986).

A large part of the discussion presented above is based on observations in the Lick/IDS system (Worthey et al. 1994, hereafter W94, and references therein), a set of 21 absorption-line indices from 4100 to 6300 Å. Based on high-quality data in that wavelength region, and stable stellar population models we are left with the puzzling result that there is large scatter in the luminosity-weighted mean age of the elliptical galaxies (e.g. T00). On the other hand the colour–magnitude relation at $z = 0.8$ continues to exist (Ellis et al. 1997; Stanford et al. 1997), indicating that at least a large fraction of elliptical galaxies in the local universe are coeval. However, an unambiguous analysis of the stellar populations has been hampered by the fundamental age–metallicity degeneracy, i.e. the two effects cannot be fully separated in the integrated spectrum of a composite stellar population. Some newer, blue indices (Jones & Worthey 1995; Worthey & Ottaviani 1997, hereafter WO97; Vazdekis & Arimoto 1999, hereafter VA99; Gorgas et al. 1999) could contribute to alleviate this situation.

In this set of papers we have increased the wavelength region that can be studied, adding the tools to analyse a few important absorption lines in the near-infrared. In fact, by extending the spectral coverage, we increase our stellar population analysis constraining power, since the contribution of different types of stars to the total luminosity varies as a function of the spectral range. Furthermore, contrary to the ultraviolet region, where a large fraction of the light can originate from just a few stars (e.g. Ponder et al. 1998), most of the stars contribute to the near-infrared Ca II triplet lines. Thanks to the large stellar library and state-of-the-art evolutionary models provided in this series of papers, observers will now be able to analyse more accurately their galaxy Ca II triplet measurements, and compare them with the models that fit in the blue.

The Ca II triplet is one of the most prominent features in the near-IR spectrum of cool stars and its potential to study the properties of stellar populations has been extensively acknowledged in the literature. For instance, the Ca II triplet strength has been found to correlate with globular cluster metallicity and, therefore, it has been proposed as a metallicity indicator for old and coeval stellar populations for the metallicity regime typical of galactic globular clusters (Armandroff & Zinn 1988, hereafter AZ88). This relation has been recalibrated by Rutledge, Hesser & Stetson (1997), who review the different methods used to measure cluster metallicities using this feature. Terlevich, Díaz & Terlevich (1990a) found that active galaxies exhibit Ca II triplet strengths equal to or larger than those found in normal ellipticals, which they interpreted as being a result of the presence of red supergiant stars in the central regions of these galaxies. The same approach has been followed by a number of authors (Forbes, Boisson & Ward 1992; García-Vargas et al. 1993; González Delgado & Pérez 1996a,b; Heckman et al. 1997; Pérez et al. 2000). The suggested gravity sensitivity of the Ca II triplet has also been proposed to constrain the dwarf/giant ratio in early-type galaxies (e.g. Cohen 1978; Faber & French 1980; Carter, Visvanathan & Pickles 1986; Alloin & Bica 1989). This feature has been measured in extensive galaxy samples (e.g. Cohen 1979; Bica & Alloin 1987; Terlevich et al. 1990b; Houdashelt 1995). Among the most interesting results derived from these studies is the fact that the Ca II triplet strength does not seem to vary much among early-type galaxies of different types, colours and luminosities. This result is at odds with the strong metallicity correlation found for the globular clusters. We refer the reader to Section 2 of Paper I for a review of previous works on the subject.

A reliable analysis of the Ca II triplet measurements in integrated spectra rests on the comparison of the data with the predictions of stellar population models. The accuracy of such predictions is highly dependent on the input calibration of the Ca II triplet line-strengths in terms of the main atmospheric stellar parameters, namely effective temperature, surface gravity and metallicity. Such calibrations have been either theoretical, based on model atmospheres, with their associated uncertainties (e.g. Smith & Drake 1987, 1990; Erdelyi-Mendes & Barbuy 1991; Jørgensen, Carlsson & Johnson 1992; Chmielewski 2000), or based on empirical stellar libraries with a poor coverage of the atmospheric parameter space (e.g. Jones, Alloin & Jones 1984; Díaz, Terlevich & Terlevich 1989; Zhou 1991; Mallik 1994, 1997; Idiart, Thévenin & de Freitas Pacheco 1997, hereafter ITD). For a more detailed discussion of these calibrations see Papers I and III. The quality of this calibration has been the major drawback of previous stellar population models that have included predictions for the strength of the Ca II triplet feature (Vazdekis et al. 1996, hereafter V96; ITD; Mayya 1997; García-Vargas, Mollá & Bressan 1998; Mollá & García-Vargas 2000, hereafter MGV). In this work we solve for these deficiencies by updating our model predictions on the basis of the ample near-IR empirical stellar spectral library and calibrations presented in Papers I–III. Therefore, this library constitutes the main ingredient of these new models.

Although this paper is not the first to present models for the Ca II triplet in integrated stellar systems, it is the first to present integrated spectra at intermediate resolution on the basis of an extensive empirical stellar library. Bruzual & Charlot (in preparation) present spectra in this wavelength region based on the theoretical library

of Lejeune, Cuisinier & Buser (1997) or the observed library of Pickles (1998), both at a resolution of 10–20 Å, i.e. an order of magnitude larger than our models. On the other hand, Schiavon, Barbuy & Bruzual (2000, hereafter SBB) predicted SSP spectra at high resolution employing a theoretical stellar library.

We must bear in mind that the empirical library used here, as well as any empirical library, implicitly includes the chemical enrichment history of the solar neighbourhood. For instance, current models use scaled-solar abundance ratios. However, there are indications that the Ca abundance is not enhanced compared with Fe in elliptical galaxies (O'Connell 1976; Vazdekis et al. 1997, hereafter V97; MGV; Peletier et al. 1999; Vazdekis et al. 2001a, hereafter V01A; PS02). This discrepancy did mostly show up when investigating the Ca 4227 line, which seems to tracks Fe lines in galaxies. Nucleosynthesis theory (Woosley & Weaver 1995) predicts that Ca is an α-element, i.e. is mainly produced in Type II supernovae and therefore should follow Mg.

The stellar population model that we describe in this paper is an improved version, as well as an extension to the near-IR spectral range, of the model presented in V96 and Vazdekis (1999, hereafter V99). Among the major changes introduced here, apart of the stellar library, is the implementation of two new IMF-shapes by Kroupa (2001, hereafter K01) (see Section 2.1), the inclusion of the new scaled-solar isochrones of the Padova group (Girardi et al. 2000, hereafter G00) (see Section 2.2), and the transformation of their theoretical parameters to the observational plane (i.e. fluxes and colours) on the basis of almost fully empirical photometric stellar libraries, such as that of Alonso, Arribas & Martínez-Roger (1999) (see Section 2.3). We also have significantly improved the way in which we grid our stellar library to compute a stellar spectrum of a given set of atmospheric parameters (see Section 3). A full description of the behaviour of the Ca II triplet in SSPs of ages greater than 1 Gyr is provided in Section 4, whilst in Section 6 we extend our model predictions to some younger stellar populations, where the asymptotic giant branch (AGB) contribution to the total luminosity in this spectral range is very important. In Section 5 we discuss the behaviour of the Ca II triplet feature as a function of the spectral resolution and galaxy velocity dispersion. Detailed comparisons with previous papers are made in Section 7. In Section 8 we establish the validity of these new models by making a direct comparison with galactic globular clusters and with two galaxies of very different luminosities. We use NGC 4478 and 4365, for which we have data both in the Ca II triplet spectral region and in the blue (V01A). A detailed analysis of galaxy spectra, however, is given in Cenarro et al. (2003, hereafter C03), in which we present new Ca II triplet data for a large sample of elliptical galaxies, and show to what extent our view of the stellar populations in elliptical galaxies may change as a result of the indices in this wavelength region. In Section 9 we give our conclusions. Finally, we provide three appendices with further details on the model construction as well as an analysis of the main uncertainties affecting our model predictions.

2 THE MODELS

The predictions that we present in this paper for the near-IR spectral range are calculated on the basis of the evolutionary stellar population synthesis model presented in V96 and V99. In this section we describe the main ingredients of these models, stressing those updates that have been performed since the original version. In Section 2.1 we summarize the IMF types used by our models and introduce two new IMF shapes considered in this paper. In Section 2.2 we describe the properties of the new isochrones of G00 that are employed here, showing the relevant differences with respect to those used in V96 (mostly Bertelli et al. 1994, hereafter B94). In Section 2.3 we describe how we transform the theoretical parameters of these isochrones to the observational plane, which is performed on the basis of extensive empirical stellar libraries rather than using model stellar atmospheres. Finally, in Section 2.4 we provide a brief summary of the main predictions of our models.

2.1 The initial mass function

In this paper we adopt the IMF shapes described in V96 (i.e. unimodal and bimodal) and the two IMFs recently introduced by K01. To calculate the number of stars in the mass interval m to $m + \mathrm{d}m$ we use the following analytical approaches for the IMF.

(i) *Unimodal:* a power-law function characterized by its slope μ as a free parameter

$$\Phi(m) \propto m^{-(\mu+1)}. \quad (1)$$

It is worth noting that the Salpeter (1955) IMF corresponds to $\mu = 1.3$.

(ii) *Bimodal:* similar to the unimodal IMF for stars with masses above 0.6 $\mathrm{M}_{\odot}$, but decreasing the number of the stars with lower masses by means of a transition to a shallower slope (see V96). This IMF is also characterized by the slope μ.

(iii) *Kroupa (2001) universal:* a multipart power-law IMF, which is similar to the Salpeter (1955) IMF for stars with masses above 0.5 $\mathrm{M}_{\odot}$, but with a decreasing contribution of lower masses by means of two flatter segments.

(iv) *Kroupa (2001) revised:* a multipart power-law IMF, in which the systematic effects owing to unresolved binaries on the single-star IMF have been taken into account. This IMF is steeper than the universal IMF by $\Delta\mu \sim 0.5$ in the mass range $0.08 \leqslant m < 1$ $\mathrm{M}_{\odot}$.

These IMF types are plotted in Fig. 1. Further details of the IMF definitions are given in Appendix A. We also refer the reader to V96 and K01 for a full description of these IMFs.

2.2 Isochrones

The new model makes use of the updated version of the theoretical isochrones of the Padova group (G00), whereas in V96 and V99 we used the B94 isochrones and the stellar tracks of Pols et al. (1995) for very low-mass stars ($M < 0.6$ $\mathrm{M}_{\odot}$). These isochrones cover a wide range of ages and metallicities and include the latest stages of the stellar evolution through the thermally pulsing AGB regime to the point of complete envelope ejection (employing a synthetic prescription). The G00 set has a larger age resolution for ages lower than 10 Gyr; however, the largest metallicity covered is $Z = 0.03$ (instead of $Z = 0.05$ as in B94). Hereafter we will refer to the metallicity following the relation

$$[\mathrm{M/H}] = \log(Z/\mathrm{Z}_{\odot}), \quad (2)$$

where $\mathrm{Z}_{\odot} = 0.019$ according to the reference value adopted by G00. The lower mass cut-off of the new isochrones has been extended down to 0.15 $\mathrm{M}_{\odot}$. The input physics of the isochrones have been updated with an improved version of the equation of state, the opacities of Alexander & Ferguson (1994) (which make the red giant branch, RGB, slightly hotter than in B94 isochrones, see Fig. C2) and a milder convective overshoot scheme. A helium fraction was adopted according to the relation: $Y \approx 0.23 + 2.25Z$.

It is worth noting that, although giant elliptical galaxies show non-solar abundance trends (e.g. Peletier 1989; Worthey, Faber &

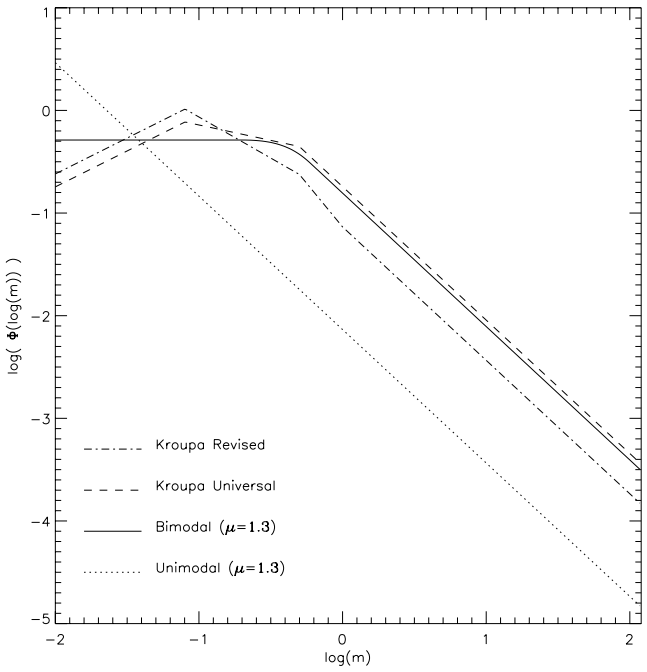

Figure 1. IMF types used by our models. Although not plotted here the slope of the power-law (μ) is allowed to vary for the unimodal and bimodal cases.

González 1992; K00; V01A), only scaled-solar abundance ratios are adopted for this set of isochrones. In particular, these galaxies seem to show an enhancement of the α-elements (e.g. O, Ne, Mg, Si, S, etc.) with respect to Fe. For a given total metallicity, the α-enhanced mixtures yield lower opacities, which translates into an increase of the temperature of the stars in the main sequence (MS) and the RGB phases (e.g. Salaris & Weiss 1998, hereafter SW98; Salasnich et al. 2000, hereafter S00; VandenBerg et al. 2000; Kim et al. 2002). Atomic diffusion is not included in the present set of isochrones, although this phenomenon decreases the temperatures of the stars of the turn-off (e.g. Salaris, Groenewegen & Weiss 2000), an effect that has been found to be useful for fitting the low line-strength values of the Balmer lines in the spectra of metal-rich globular clusters (Vazdekis et al. 2001b, hereafter V01B).

2.3 Transformation to the observational plane

To transform the theoretical parameters of the isochrones to the observational plane, i.e. colours and magnitudes, we make use of relations inferred on the basis of extensive empirical photometric stellar libraries (rather than by implementing theoretical stellar atmospheric spectra) to obtain each colour as a function of the temperature, metallicity and gravity. We use the metallicity-dependent empirical relations of Alonso, Arribas & Martínez-Roger (1996) and Alonso et al. (1999) for dwarfs and giants, respectively (each stellar sample is composed of ∼500 stars). The derived temperature scale is based on the IR flux method and, therefore, is marginally dependent on the model atmospheres. This treatment for the giants is the most important difference with respect to the models of V96, where we used the empirical calibration of Ridgway et al. (1980) to obtain the $V - K$ colour from $T_{\rm eff}$, after which we applied the colour–colour conversions of Johnson (1966). The empirical (not the theoretical) compilation of Lejeune, Cuisinier & Buser (1997, 1998) (and references therein) are used for the coolest dwarfs ($T_{\rm eff} \leqslant$ 4000 K) and giants ($T_{\rm eff} \leqslant$ 3500 K), respectively, for solar metallicity; a semi-empirical approach was applied to other metallicities on the basis of these relations and the model atmospheres of Bessell et al. (1989, 1991) and the library of Fluks et al. (1994). The empirical compilation of Lejeune et al. was also used for stars with temperatures above ∼8000 K.

Finally, we use the metal-dependent bolometric correction given by Alonso, Arribas & Martínez-Roger (1995) and Alonso et al. (1999) for dwarfs and giants, respectively. For the Sun we adopt the bolometric correction $\mathrm{BC}_{\odot} = -0.12$, with a bolometric magnitude of 4.70 according to these authors.

2.4 Summary of the previous model predictions

Using data obtained at different spectral ranges, or combining spectroscopic and photometric information, increases our constraining power for interpreting the stellar populations (e.g. V97). Furthermore, the use of a set of model predictions for a given spectral range, such as those presented in this paper and those of other authors for a different spectral range, might drive to systematic effects caused by differences in the adopted model prescriptions (e.g. Charlot, Worthey & Bressan 1996). Furthermore, it is well known that the ages or metallicities inferred by means of stellar population synthesis modelling should be taken on a relative basis (e.g. V01B). Therefore, we briefly summarize below our model predictions for those interested in applying the models presented in this paper.

Broadband colours, mass-to-light ratios and line-strengths for the main features in the Lick/IDS system were predicted in V96. A new version of these models includes the Hδ and Hγ indices of WO97, as well as the break at ∼4000 Å of Gorgas et al. (1999). SSP spectral energy distributions in the blue and visible at a resolution of 1.8 Å (FWHM) were presented in V99. New Hγ index predictions can be found in VA99 and V01B. Finally, optical and near-IR surface brightness fluctuations magnitudes and colours (including the WFPC2 *Hubble Space Telescope* filter system) were presented in Blakeslee, Vazdekis & Ajhar (2001), where we include a description of the updated models. All these predictions are available at the web page: http://www.iac.es/galeria/vazdekis/.

3 NEW MODEL PREDICTIONS FOR THE NEAR-INFRARED

Using the model ingredients described in Section 2 and the new stellar spectral library presented in Papers I and II, we follow two different approaches to build up two sets of model predictions. First, we compute spectral energy distributions at a resolution (FWHM = 1.5 Å) for different metallicities, ages and IMFs. In Section 3.1 we further the preparation of our stellar library for stellar population synthesis modelling, whereas in Section 3.2 and Appendix B we describe our model and computing details. In Appendix C we describe some tests that we have performed to show the main uncertainties affecting the obtained model predictions, as well as to probe the robustness of our approach. For the second set of model predictions, which is described in Section 3.3, we make use of the empirical fitting functions presented in Paper III (based on the same stellar spectral library) to calculate the strengths of the Ca II triplet feature by means of the index definitions given in Paper I. Finally, in Section 3.4 we summarize these two sets of model predictions and describe the spectral properties and parameter coverage of the synthesized SSP spectral energy distributions.

3.1 The near-IR empirical stellar spectral library

The main ingredient of the models presented in this paper is a new stellar library covering the spectral range around the near-IR Ca II

triplet feature at a resolution of 1.5 Å (FWHM). A full description of this library was given in Paper I, where we also propose a new index definition for this feature (i.e. CaT*). In order to make this stellar library useful for stellar population synthesis modelling, we require a homogeneous set of accurate atmospheric parameters ($T_{\rm eff}$, log g, [Fe/H]) for the stellar sample (see Paper II). As pointed out in V99, this step is particularly important to avoid systematic trends in the parameters among different authors. In this section we give further details on the preparation of the stellar library for its implementation in the model. This requires us to identify those stars for which the spectra might not be properly representing a given set of atmospheric parameters (Section 3.1.1). Another important step is the characterization of the parameter coverage of the stellar library. This step, which is described in Section 3.1.2, allows us to understand the limitations of the models presented in Section 3.

3.1.1 Preparation of the stellar library

To optimize the stellar library we have performed a second selection on the stars to use for the stellar population modelling. For this purpose we identified all the spectroscopic binaries, making use of the SIMBAD data base, as well as those stars with high signal of variability ($\Delta V > 0.10$ mag). We used the Combined General Catalogue of Variable Stars from Kholopov et al. (1998) (the electronically readable version is provided at CDS). Moreover, we removed from the sample a number of stars that were found to be irrelevant since the stellar library contains a reasonably large number of stars with similar atmospheric parameters with no such high variability feature. The removed stars were: HD 10476, 36079, 113139, 113226, 125454, 138481, 153210 and 205435. We refer the reader to Section 3.2.2 and Appendix B for a full description of how we deal with these stars when calculating a representative stellar spectrum for a given set of atmospheric parameters.

A number of stars were removed owing to the high residuals obtained when calculating the Ca II triplet fitting functions (see Paper III). These stars were: HD 17491, 35601, 42475, 115604, 120933, 121447, 138279, 181615, 217476 and 222107.

We did remove from the original stellar sample most of the stars for which at least one of the three atmospheric parameters was lacking (see table 5 of Paper II). However, we kept 47 of these stars, with unknown metallicities, but for which the temperatures were either larger than 9000 K or smaller than 4000 K.

We are interested in achieving the largest possible spectral resolution for our model predictions, i.e. FWHM = 1.5 Å. We therefore removed from the library the few stars observed with instrumental configurations providing ∼2.1 Å, as described in table 2 of Paper I (i.e. those corresponding to observing runs 5 and 6). These stars were those corresponding to NGC 188 as well as NGC 7789 676, 7789 859, 7789 875, 7789 897 and 7789 971. The remaining stars, for which spectra were obtained at resolutions slightly better than 1.5 Å, were broadened to match this resolution (see Paper I).

For different technical reasons we removed from the sample an additional number of stars. In particular, a subset of stars were discarded because their spectra were of low signal-to-noise ratio (i.e. M5 II-53, M92 I-10 and M92 XII-24). M71 1-63 and HD 232979 were removed for being affected by cosmic rays and M67 F119 for the poor flux calibration quality.

As a result of this cleaning process we obtained a subsample composed of 616 stars. A final step was to revise the atmospheric parameters presented in Paper II for a number of stars. This is motivated by the evidence that their line-strength values deviate significantly from the expected general trends predicted by the fitting functions. In particular, we modified the $T_{\rm eff}$ of HD 167006 from 3470 to 3650 K in order to bring it in better agreement with the value predicted by a new set of fitting functions, which calculates the slope of the spectrum around the Ca II triplet feature owing to the TiO molecular bands (Cenarro 2002). Finally, we also changed the metallicity adopted for the stars of M71 from −0.70 (Carretta & Gratton 1997) to −0.84 in order to achieve a better agreement with the predictions of the fitting functions presented in Paper III for the Ca II triplet feature. As described in Section 3.3 of Paper III, the stars of this globular cluster showed systematic residuals in comparison with the strengths predicted by the fitting functions (i.e. Δ CaT* = −0.35), which translates to the metallicity value that we adopt here. We refer the reader to that paper for an extensive discussion on the subject.

3.1.2 Stellar atmospheric parameter coverage

Fig. 2 shows the parameter coverage of the selected subsample of stars. The adopted values for the $T_{\rm eff}$, log g and [Fe/H] of the stars of our sample were extensively discussed in Paper II. This figure includes the corrections described in Section 3.1.1. The figure shows that all types of stars are well represented for solar metallicity. We also see a good coverage of typical dwarfs and giants of $5000 < T_{\rm eff} < 6500$ K and $4000 < T_{\rm eff} < 5500$ K, respectively, for metallicities in the range $-0.7 \leqslant$ [Fe/H] $\leqslant +0.2$.

Unfortunately, very metal-rich stars, particularly dwarfs, are scarce in the sample, preventing us from providing predictions for SSPs of metallicities greater than +0.2. We also note that very cool dwarfs and giants of non-solar metallicity are scarce. These dwarfs are particularly useful for predicting stellar populations with very steep IMFs, i.e. dwarf-dominated, whereas the effect of these low-metallicity giants will be discussed below. An important gap is the absence of metal-poor dwarfs of $T_{\rm eff} > 6500$ K. The lack of these stars does not allow us to predict SSPs of ages younger than ∼6 Gyr for [Fe/H] ∼ −0.7 and younger than ∼2.5 Gyr for [Fe/H] ∼ −0.4, since they will be representing the predicted turnoff for these stellar populations. Overall we conclude that the metallicity range where

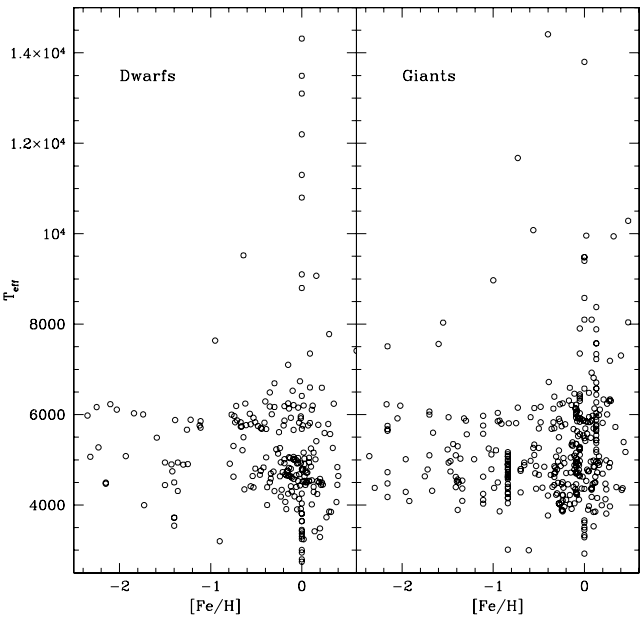

Figure 2. The fundamental parameter coverage of the subsample of selected stars.

we are mostly safe is $-0.7 \leqslant$ [Fe/H] $\leqslant +0.2$. With more caveats we also can predict stellar populations for lower metallicities where the contribution of dwarf stars with temperatures above $T_{\rm eff} > 6500$ K is not significant, and the horizontal branch is not too blue (note in Fig. 2 the lack of metal-poor giants with temperatures greater than ∼6000 K). Therefore, in this metallicity range we mostly need to focus on SSPs with ages greater than ∼10 Gyr, but less than ∼13 Gyr.

3.2 Spectral synthesis of SSPs

Predicting spectral energy distributions for stellar populations at intermediate or moderately high resolution, rather than the strengths of a given number of features (see Section 3.3), requires a complete stellar spectral library where all type of stars are well represented, and for which the spectra are of high quality and flux calibrated. Theoretical libraries are difficult to achieve owing to the limitations of the input physics and the computing power. On the other hand, the empirical libraries actually suffer from the difficulties in observing a good number of representative stars of all types for which the atmospheric parameters are accurately known. Spectral energy distributions at very low resolutions for stellar populations covering a large range of ages and metallicities were predicted, either based on the Kurucz (1992) theoretical stellar library (e.g. Bressan, Chiosi & Fagotto 1994; Kodama & Arimoto 1997; Kurth, Fritze-V. Alvensleben & Fricke 1999; Poggianti et al. 2001) or empirical stellar libraries (Bruzual & Charlot 1993). However, the low dispersion of the predicted spectra did not allow us to measure reliable line-strengths.

More recently, the availability of such libraries at higher dispersion has made it possible to follow the spectral synthesis approach for the blue spectral range. In V99, we used the extensive empirical stellar library of Jones (1999), composed of more than 600 stars, to predict spectra of SSPs at a resolution of 1.8 Å (FWHM). This approach allowed us to analyse the entire spectrum of a galaxy at one time and to measure line-strengths at the resolution imposed by the instrumental configuration of the observational data, or to galaxy internal velocity dispersion. This represents a great advantage over previous models, such as those of Worthey (1994) or V96, that only predicted the strengths of a given number of features under a determined instrumental configuration and resolution, i.e. the Lick/IDS system (Gorgas et al. 1993; W94). Note that the old models required the observers to transform their data to the characteristics of the model predictions. A different approach was followed by SBB, who synthesized SEDs of SSPs for the near-IR spectral range on the basis of a fully synthetic stellar spectral library by SBB. In the following, we describe in detail how we make use of our stellar library for predicting near-IR spectra at a resolution of 1.5 Å (FWHM) for SSPs of different ages, metallicities and IMF slopes. Although we have followed a procedure similar to that of V99 for the optical spectral range we have updated the method as described below.

To predict any integrated observable (e.g. colours, line-strengths, SEDs) of an SSP of age t and metallicity [M/H] the synthesis code yields a stellar distribution on the basis of the adopted isochrones and IMF (see V96 for more details). Therefore, the integrated spectrum of the SSP, $S_\lambda(t, [{\rm M/H}])$, is calculated in the following way:

$$S_\lambda(t, [{\rm M/H}]) = \int_{m_{\rm l}}^{m_{\rm t}} S_\lambda(m, t, [{\rm M/H}]) N(m, t) \times F_{\Delta\lambda_{\rm ref}}(m, t, [{\rm M/H}])\, {\rm d}m, \quad (3)$$

where $S_\lambda(m, t, [{\rm M/H}])$ is the empirical spectrum corresponding to a star of mass m and metallicity [M/H] that is alive at the age assumed for the stellar population t. $F_{\Delta\lambda_{\rm ref}}(m, t, [{\rm M/H}])$ is its corresponding absolute flux at a certain wavelength reference interval, $\Delta\lambda_{\rm ref}$, and $N(m, t)$ is the number of this type of stars, which depends on the adopted IMF. $m_{\rm l}$ and $m_{\rm t}$ are the stars with the smallest and largest stellar masses, respectively, which are alive in the SSP. The upper mass limit depends on the age of the stellar population.

The spectrum to be assigned to each of the stars required by equation (3) is selected from the empirical stellar data base, whereas the corresponding absolute flux is assigned following the prescriptions of our code, which are based on the extensive empirical photometric stellar libraries described in Section 2.3. In Sections 3.2.1 and 3.2.2 we describe how we calculate $F_{\Delta\lambda_{\rm ref}}(m, t, [{\rm M/H}])$ and $S_\lambda(m, t, [{\rm M/H}])$, respectively.

3.2.1 Assigned stellar flux

We need to find a common reference wavelength interval, $\Delta\lambda_{\rm ref}$, from which we can scale $S_\lambda(m, t, [{\rm M/H}])$. We selected for this purpose the spectral range λλ8475–8807 around the peak of the *I* filter of Johnson (1966). We have chosen the Johnson (1966) *I* filter because its effective wavelength is closer to the spectral range covered by our stellar spectra than the *I* filter of the Cousins system (Bessell 1979). We divide our stellar spectra by the average flux in the selected wavelength reference interval. To calculate the absolute flux in this spectral region for each of the stars requested by the code, $F_{\Delta\lambda_{\rm ref}}(m, t, [{\rm M/H}])$, we first used equation (6) of Code et al. (1976), which provides a relation between the absolute V flux and the calibrated bolometric correction in order to infer equation (2) of V99 from which we derive the following relation:

$$\frac{F_I}{F_{{\rm bol}_\odot}} = \frac{10^{+0.4(V-I)}}{10^{+0.4(M_V-3.762)}}, \quad (4)$$

where F_I is the absolute flux in the Johnson *I* band. The next step is to calculate the absolute flux per angstrom in the selected reference interval:

$$F_{\Delta\lambda_{\rm ref}} = \frac{f_n F_I}{\Delta\lambda_{\rm ref}}, \quad (5)$$

where f_n represents the fraction of F_I corresponding to the normalization wavelength interval, i.e. $\Delta\lambda_{\rm ref} = 8475$–$8807$ Å. This factor is calculated on the basis of the empirical stellar spectral library of Pickles (1998), for which we have compared the flux in the *I* filter and in the normalization region, obtaining the following relations

$$\begin{aligned} f_n &= -1.620\,675 + 0.496\,916 \log T_{\rm eff}, \log T_{\rm eff} < 3.55, \text{ dwarfs} \\ f_n &= -0.163\,463 + 0.086\,852 \log T_{\rm eff}, \log T_{\rm eff} < 3.55, \text{ giants} \\ f_n &= +0.156\,952 - 0.003\,324 \log T_{\rm eff}, \log T_{\rm eff} \geqslant 3.55. \end{aligned} \quad (6)$$

Note that f_n is nearly constant, except for M stars with temperatures lower than ∼3500 K (see Fig. 3).

Fig. 4 illustrates the contributions of the different evolutionary phases to $S_\lambda(t, [{\rm M/H}])$ in the selected normalization wavelength interval, according to the values calculated for $F_{\Delta\lambda_{\rm ref}}$ for each star. The figure shows the fraction of luminosity (as a percentage) of these evolutionary stages for SSPs of several IMF slopes (unimodal), metallicities and ages. The RGB, MS and HB are the main contributors to this spectral range. The weight of the AGB decays very rapidly as the stellar population evolves, whereas the RGB is completely built up when the age reaches ∼2 Gyr. The contribution of the subgiant branch (SGB) is the smallest one in all the diagrams. The effect of the IMF is mostly reflected in the relative contribution of the MS and RGB.

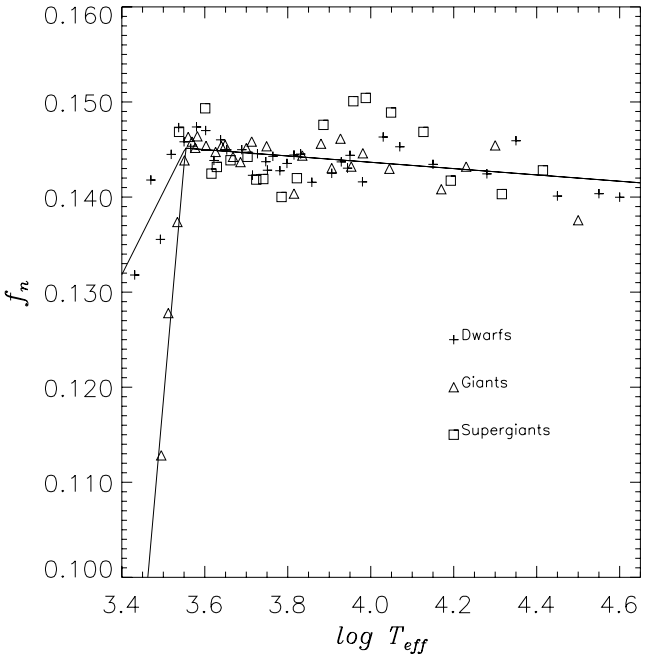

Figure 3. Normalization wavelength interval flux correcting factor versus log $T_{\rm eff}$. The fit is given in equation (6).

Finally, it is worth recalling that the fact that the effective wavelength of the Johnson *I* filter experiments with a significant shift as a function of the spectral type, makes our scaling approach more secure than if we had chosen, as a reference interval, a significantly narrower spectral range. In fact, we have tested to scale the stellar spectra with F_I (i.e. non-corrected by f_n), selecting as a normalization region either the pseudocontinuum λλ8474–8484 (i.e. *c*1, see Table 1) or 8776–8792 Å (i.e. *c*5). For the synthesized SSP spectrum, e.g. for 12.6 Gyr and solar metallicity, the slope of the continuum in the wavelength range λλ8500–8850 (measured as $\rm flux_{c5}/flux_{c1}$) varies by ∼4 per cent, and the value of the CaT* index by ∼0.14 Å (which represents ∼2 per cent of the index strength). This effect is a result of the fact that the selection of a redder continuum emphasizes the contribution of redder stars in equation (3).

3.2.2 Adopted stellar spectrum

In Appendix B we describe the method that we have followed for obtaining from the whole subsample of selected stars, a representative spectrum, $S_\lambda(m, t, [\rm M/H])$, for a given set of atmospheric parameters θ, log *g* and [M/H]. It is worth noting that rather than $T_{\rm eff}$ we have chosen to work with θ ($\equiv 5040/T_{\rm eff}$) in order to follow the scale adopted in Paper III for calculating the empirical fitting functions for the Ca II triplet feature. We have tested, however, that using this parameter does not affect the resulting integrated SSP spectrum.

Basically our approach consists in finding all the stars for which the parameters are enclosed within a given box in the three-parameter space. The method ensures the presence of stars in several directions to alleviate the effect of asymmetries in the distribution of stars around the point. For example, for metallicities greater than solar, more stars are usually found with lower, rather than higher, metallicity. The size of the selected finding box is taken to be a function of the density of stars around the requested point, i.e. the larger the density is the smaller the box. Moreover, in the more populated parameter regions, the typical uncertainties in the determination of the atmospheric parameters are usually smaller than in regions with lower densities (see Paper II), in agreement with the adopted criterion. When needed, the starting box is enlarged until suitable stars are found.

The obtained stars are combined according to their parameters θ, log *g* and [M/H] and to the signal-to-noise ratio of their spectra. However, the method ensures that spectroscopic binaries and stars with anomalous signatures of variability do not significantly contribute to the average spectrum. Finally, we apply a minimal correction to these weights in order to ensure the obtention of a spectrum for which the atmospheric parameters match the requested ones.

3.3 Line-strength index synthesis

The most widely employed approach for modelling and studying stellar populations using absorption lines is based on the, so-called, empirical fitting functions. These functions describe the strength of, previously defined, spectral features in terms of the main atmospheric parameters. These calibrations are directly implemented into the stellar population models to derive the index values for stellar populations of different ages, metallicities and IMFs. The main advantage of this approach over the spectral synthesis, which provides full spectra, is that the latter method relies on the availability of a complete stellar library at the appropriate spectral resolution. The difficulties in achieving such libraries in the most recent past made the fitting function method the only possible approach to provide robust diagnostics for the stellar populations (e.g. Buzzoni 1993; Worthey 1994; V96; Tantalo, Chiosi & Bressan 1998; Kurth et al. 1999; Maraston & Thomas 2000; Poggianti et al. 2001; Bruzual & Charlot in preparation). The predictions based on these models have been widely used over the last decade (see Trager et al. 1998 for an extensive review).

In the blue and visible part of the spectrum, we predicted in V96 the most important absorption line-strengths of the Lick/IDS system, at intermediate resolution FWHM ∼9 Å. We used the empirical fitting functions of Gorgas et al. (1993), W94 and WO97. Moreover, we also predicted in that paper the strengths of the Ca II triplet on the basis of the stellar spectral library and the index definition of Díaz et al. (1989). Ca II triplet strengths were also calculated by García-Vargas et al. (1998), MGV and ITD (see Section 7 for a full comparison with these models). It is worth noting that the use of these predictions requires one to adapt the data to the characteristics of the instrumental-dependent stellar spectral library employed by these models (see WO97 for an extensive review of the method).

Since we now have a better stellar library and models, our previous predictions for the Ca II triplet presented in V96 are superseded by those calculated in this section. Here we adopt for the Ca II triplet feature the index definition given in Paper I (CaT*). This new index removes the H Paschen lines contamination and it is, therefore, a reliable indicator of pure Ca II triplet strength. The index is given by $\rm CaT^* = CaT - 0.93\ PaT$, where the CaT and PaT indices measure the strengths of the raw calcium triplet and of three pure H Paschen lines, respectively (see Table 1). All of these indices are computed for a nominal resolution of FWHM = 1.5 Å. Further details, as well as relations to transform this index to other popular definitions for the Ca II triplet feature can be found in Paper I.

Empirical fitting functions for the CaT and PaT indices were calculated in Paper III. These functions are polynomials that relate the strength of these indices to the stellar atmospheric parameters (θ, log *g*, [M/H]) derived in Paper II. The new fitting functions reveal

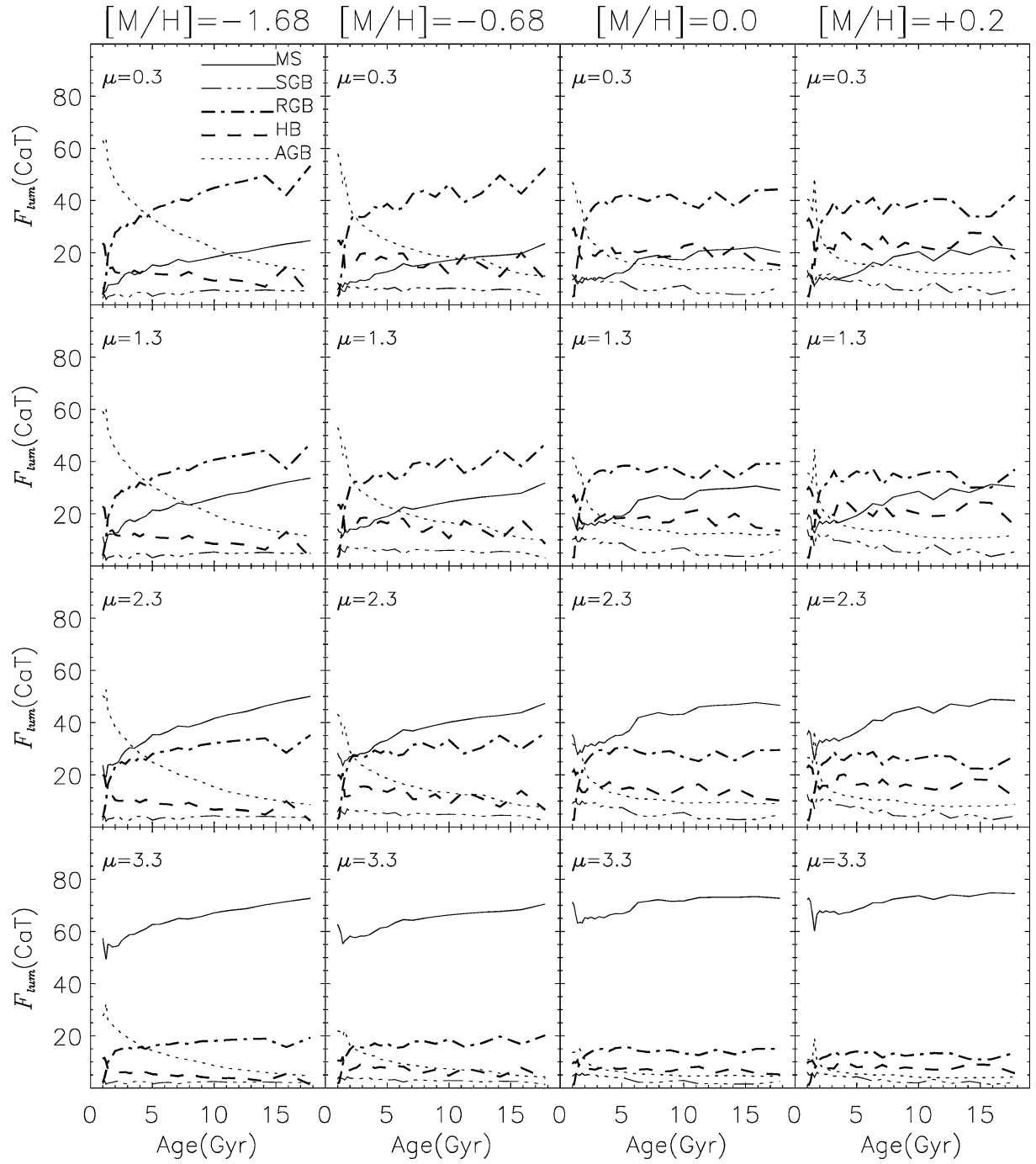

Figure 4. Fraction of luminosity (as a percentage) of the different stellar evolutionary phases in the Ca II triplet spectral region for SSPs of unimodal IMF of different slopes (from top to bottom panels), metallicities (from left- to right-hand panels) and ages (in each panel).

Table 1. Bandpass limits for the generic indices CaT and PaT.

CaT central bandpasses (Å)	PaT central bandpasses (Å)	Continuum bandpasses (Å)
Ca1 8484.0–8513.0	Pa1 8461.0–8474.0	*c*1 8474.0–8484.0
Ca2 8522.0–8562.0	Pa2 8577.0–8619.0	*c*2 8563.0–8577.0
Ca3 8642.0–8682.0	Pa3 8730.0–8772.0	*c*3 8619.0–8642.0
		*c*4 8700.0–8725.0
		*c*5 8776.0–8792.0

a complex behaviour of the Ca II triplet features as a function of the atmospheric parameters. In particular, for hot and cold stars, the temperature and luminosity class are the main driving parameters, whereas, in the mid-temperature regime, the three atmospheric parameters play an important role. Among the advantages of the new fitting functions over previous predictions is that they include the whole range of effective temperatures and, in particular, cold stars. We refer the interested reader to Paper III for a full description of these functions.

Table 2. Spectral properties and parameter coverage of the synthesized model SEDs.

Spectral properties	
Spectral range	λλ8348.85–8950.65
Spectral resolution	FWHM $= 1.5$Å, $\sigma = 22.2$ km s^{-1}
Linear dispersion	0.85Å pixel^{-1} (29.358 km s^{-1})
Continuum shape	Flux-scaled
SSPs parameter coverage	
IMF type	Unimodal, bimodal, Kroupa universal, Kroupa revised
IMF slope (for unimodal and bimodal)	0.3–3.3
Metallicity	−1.68, −1.28, −0.68, −0.38, 0.0, +0.20
Age ([M/H] < −0.68)	$10.0 \leqslant t \leqslant 17.78$ Gyr
Age ([M/H] = −0.68)	$5.62 \leqslant t \leqslant 17.78$ Gyr
Age ([M/H] = −0.38)	$2.51 \leqslant t \leqslant 17.78$ Gyr
Age ([M/H] = 0.0)	$0.1 \leqslant t \leqslant 17.78$ Gyr
Age ([M/H] = +0.2)	$1.0 \leqslant t \leqslant 17.78$ Gyr

The implementation of these fitting functions in our stellar population code is readily done as follows. A flux-weighted index i for a SSP of age (t) and metallicity ([M/H]) is given by

$$i_{\rm SSP} = \frac{\int_{m_{\rm l}}^{m_{\rm t}} i(m,t,[{\rm M/H}])N(m,t)F_{\Delta\lambda_{\rm ref}}(m,t,[{\rm M/H}])\,{\rm d}m}{\int_{m_{\rm l}}^{m_{\rm t}} N(m,t)F_{\Delta\lambda_{\rm ref}}(m,t,[{\rm M/H}])\,{\rm d}m}, \qquad (7)$$

where the flux $F_{\Delta\lambda_{\rm ref}}(m,t,[{\rm M/H}])$ is used to scale the contribution of a star of mass m and age t in a given evolutionary stage. We adopt the flux corresponding to the scaling wavelength interval used for the spectral synthesis, i.e. $\Delta\lambda_{\rm ref}$, since it is centred on these features.

3.4 Summary of the new model predictions for the near-IR

In this section we summarize the new model predictions presented here for the near-IR spectral range. There are two main products that are interesting for the stellar population analyses: (i) the spectral library for SSPs, for which we list in Table 2 the main properties of the synthesized SSP spectra, as well as the model parameters coverage according to the limitations described in Section 3.1.2 and (ii) the CaT*, CaT and PaT index strengths predicted on the basis of the empirical fitting functions, which are listed in Table 3. It is worth noting that the index values given in this table for SSPs of different ages, metallicities and IMF types and slopes, are calculated at a resolution of 1.5 Å (FWHM). Therefore, users interested in applying these predictions should correct their index measurements to those they would have obtained at the resolution of the models presented here (see the relations given in Section 5).

These two sets of model predictions can either be obtained from the authors or from the following web pages: http://www.ucm.es/info/Astrof/ellipt/CATRIPLET.html, http://www.nottingham.ac.uk/~ppzrfp/CATRIPLET.html, and http://www.iac.es/galeria/vazdekis/.

4 THE BEHAVIOUR OF THE CA II TRIPLET FEATURE IN SSPS

In this section we focus on describing the behaviour of the integrated Ca II triplet feature as a function of the relevant stellar population parameters in old-aged SSPs. In Section 6 we will present a discussion for some younger ages. We also discuss here some of the main differences seen in the full spectra predicted by the models, but we refer the reader to C03 and Cenarro (2002), for a detailed description of the behaviour of other features and the slope of the characteristic continuum around the Ca II triplet feature, which is largely determined by the contributions of the TiO molecular bands. In Section 4.1 we describe the time evolution of the Ca II triplet feature and its dependence on metallicity, whereas in Section 4.2 we discuss the effects of the IMF.

4.1 The effects of the age and metallicity

In Fig. 5 we plot the time evolution of the CaT* index as calculated on the basis of the fittings functions of Paper III (see Section 3.3) and as measured on the synthesized spectra (Section 3.2). The two set of predictions are given at a resolution of 1.5 Å (FWHM), i.e. $\sigma = 22.2$ km s^{-1} (the behaviour of the Ca II triplet feature as a function of spectral resolution will be discussed in Section 5). Fig. 5 reveals three major features: (i) the strength of the CaT* index does not vary much for stellar populations older than ∼3 Gyr, for all metallicities, (ii) there is a strong sensitivity of the CaT* index as a function of metallicity for values below [M/H] ∼ −0.5 and (iii) for higher metallicities, the CaT* index does not show any significant dependence on the metallicity and the strength of this feature tends to saturate.

The observed saturation of the CaT* index can be understood in terms of comparing the contributions of the MS and RGB with the total luminosity of an SSP in this spectral range (see Fig. 4). If we focus on the second row of panels of this figure, i.e. for $\mu = 1.3$ (we will discuss the effects of the IMF in Section 4.2), we see that the relative contribution of the MS with respect to the RGB becomes larger as the metallicity increases. Dwarf stars provide smaller strengths for this feature than giants according to the results obtained in Paper III. Moreover, in metal-rich SSPs the RGB is populated with an increased fraction of very cool stars. For temperatures cooler than ∼3500 K, the CaT* index does not depend on metallicity and decreases very rapidly with decreasing temperature (see fig. 7 of Paper III). The saturation of the Ca II triplet for large metallicities is a result that differs from the predictions of previous authors (see Section 7). This result might be supported by the CaT* index measurements obtained for a large sample of ellipticals (C03) and bulges of spirals (Falcón-Barroso et al. 2002), as well as for the most metal-rich galactic globular clusters (see Section 8.1). Furthermore, Cohen (1979), Bica & Alloin (1987), Terlevich et al. (1990b) and Houdashelt (1995) found that the strength of the Ca II triplet did not vary much among early-type galaxies of different absolute magnitudes and colours.

Fig. 5 shows a reasonably good agreement between our CaT* index predictions based on the empirical fitting functions and those measured on the synthesized spectra. We note, however, a better agreement for larger metallicities, where the CaT* strengths provided by the spectral synthesis are marginally larger than those predicted on the basis of the empirical fitting functions. For [M/H] = −0.38 and −0.68, the spectral synthesis approach provides smaller CaT* values, and the obtained differences between the predictions based on the two approaches can be as large as 0.2 Å (i.e. ∼3 per cent of the CaT* index value) for [M/H] = −0.68. Also, the SSP spectra for [M/H] = −1.28 and −1.68 provide smaller CaT* strengths than the values obtained on the basis of the fitting functions, although the observed differences are smaller than those obtained for [M/H] = −0.68. These differences must be attributed to differences in the methods employed by the two approaches to provide, for a

Table 3. Predicted CaT* and PaT indices for SSPs of different ages and metallicities (indicated in the first two columns) for different IMF shapes and slopes (μ): unimodal, bimodal (according to the definitions given in V96) and the universal and revised IMFs of K01 (see Section 2.1 and Appendix A). The Salpeter (1955) solar neighbourhood IMF is given by a unimodal IMF of slope 1.3. The tabulated index values were calculated on the basis of the empirical fitting functions given in Paper III (see Section 3.3). The spectral resolution is 1.5 Å (FWHM). The Paschen contaminated Ca II triplet index, CaT, can be easily calculated by applying the relation: CaT = CaT*+0.93 PaT (see Paper I).

		Unimodal								Bimodal				K. universal		K. revised	
[M/H]	Age	$\mu = 0.3$		$\mu = 1.3$		$\mu = 2.3$		$\mu = 3.3$		$\mu = 1.3$		$\mu = 2.3$					
	(Gyr)	CaT*	PaT	CaT*	PaT	CaT*	PaT	CaT*	PaT	CaT*	PaT	CaT*	PaT	CaT*	PaT	CaT*	PaT
−1.68	10.00	4.283	0.783	4.339	0.756	4.564	0.698	5.104	0.606	4.290	0.765	4.331	0.735	4.289	0.766	4.320	0.752
−1.68	11.22	4.257	0.737	4.326	0.710	4.568	0.658	5.115	0.582	4.272	0.718	4.321	0.690	4.271	0.719	4.307	0.705
−1.68	12.59	4.244	0.703	4.326	0.676	4.581	0.629	5.131	0.565	4.266	0.684	4.321	0.657	4.265	0.685	4.306	0.672
−1.68	14.13	4.249	0.749	4.342	0.714	4.611	0.655	5.159	0.578	4.277	0.724	4.337	0.691	4.275	0.725	4.320	0.709
−1.68	15.85	4.274	0.809	4.375	0.763	4.652	0.690	5.192	0.597	4.304	0.778	4.367	0.737	4.303	0.779	4.351	0.758
−1.68	17.78	4.327	0.855	4.434	0.801	4.714	0.715	5.235	0.610	4.358	0.820	4.420	0.774	4.356	0.821	4.406	0.797
−1.28	10.00	5.447	0.760	5.444	0.740	5.529	0.696	5.783	0.619	5.418	0.747	5.406	0.725	5.417	0.747	5.420	0.737
−1.28	11.22	5.451	0.723	5.455	0.703	5.549	0.664	5.801	0.599	5.428	0.709	5.422	0.689	5.427	0.710	5.433	0.700
−1.28	12.59	5.448	0.695	5.460	0.676	5.563	0.641	5.816	0.586	5.430	0.682	5.429	0.664	5.429	0.682	5.438	0.673
−1.28	14.13	5.443	0.678	5.463	0.659	5.574	0.626	5.829	0.577	5.431	0.665	5.436	0.646	5.430	0.665	5.442	0.656
−1.28	15.85	5.383	0.682	5.420	0.660	5.555	0.624	5.830	0.574	5.380	0.666	5.396	0.646	5.378	0.667	5.398	0.657
−1.28	17.78	5.395	0.821	5.437	0.781	5.578	0.716	5.850	0.626	5.395	0.795	5.413	0.761	5.393	0.796	5.414	0.778
−0.68	5.62	6.768	0.951	6.671	0.930	6.527	0.865	6.289	0.711	6.680	0.939	6.579	0.912	6.680	0.939	6.656	0.926
−0.68	6.31	6.807	0.913	6.711	0.892	6.564	0.830	6.314	0.690	6.722	0.900	6.624	0.874	6.722	0.900	6.694	0.888
−0.68	7.08	6.835	0.880	6.741	0.859	6.592	0.801	6.335	0.672	6.754	0.867	6.659	0.843	6.754	0.867	6.720	0.856
−0.68	7.94	6.863	0.851	6.770	0.829	6.618	0.773	6.352	0.655	6.785	0.837	6.693	0.814	6.785	0.837	6.744	0.826
−0.68	8.91	6.897	0.825	6.804	0.804	6.648	0.751	6.372	0.642	6.821	0.812	6.730	0.791	6.821	0.812	6.780	0.802
−0.68	10.00	6.925	0.803	6.832	0.783	6.672	0.732	6.389	0.630	6.851	0.791	6.762	0.771	6.851	0.791	6.810	0.781
−0.68	11.22	6.961	0.784	6.867	0.764	6.701	0.716	6.409	0.621	6.889	0.772	6.801	0.753	6.889	0.772	6.848	0.762
−0.68	12.59	6.999	0.765	6.904	0.746	6.732	0.701	6.430	0.613	6.929	0.754	6.842	0.737	6.929	0.754	6.887	0.745
−0.68	14.13	7.026	0.754	6.930	0.735	6.754	0.691	6.446	0.607	6.958	0.743	6.872	0.727	6.958	0.743	6.916	0.734
−0.68	15.85	7.033	0.745	6.937	0.726	6.759	0.684	6.452	0.603	6.967	0.735	6.885	0.720	6.968	0.735	6.925	0.726
−0.68	17.78	7.033	0.746	6.936	0.726	6.757	0.682	6.453	0.602	6.970	0.735	6.890	0.720	6.971	0.735	6.928	0.726
−0.38	2.51	7.096	1.188	6.963	1.181	6.720	1.105	6.162	0.830	6.976	1.188	6.823	1.163	6.976	1.189	6.962	1.178
−0.38	2.82	7.111	1.135	6.984	1.123	6.743	1.046	6.180	0.790	6.999	1.131	6.854	1.103	6.999	1.131	6.983	1.120
−0.38	3.16	7.140	1.074	7.014	1.058	6.768	0.982	6.193	0.746	7.031	1.066	6.890	1.037	7.031	1.067	7.012	1.056
−0.38	3.55	7.163	1.042	7.042	1.024	6.796	0.947	6.214	0.723	7.060	1.032	6.925	1.002	7.060	1.032	7.039	1.021
−0.38	3.98	7.192	1.024	7.073	1.004	6.826	0.927	6.236	0.710	7.093	1.012	6.963	0.981	7.094	1.012	7.070	1.001
−0.38	4.47	7.223	1.000	7.107	0.978	6.855	0.901	6.256	0.693	7.129	0.986	7.002	0.956	7.130	0.987	7.103	0.975
−0.38	5.01	7.232	0.973	7.114	0.948	6.855	0.870	6.249	0.670	7.140	0.957	7.015	0.926	7.140	0.958	7.109	0.945
−0.38	5.62	7.263	0.949	7.146	0.923	6.882	0.845	6.266	0.654	7.174	0.932	7.052	0.901	7.175	0.933	7.140	0.920
−0.38	6.31	7.294	0.926	7.174	0.898	6.897	0.821	6.268	0.637	7.205	0.908	7.082	0.877	7.206	0.909	7.166	0.896
−0.38	7.08	7.276	0.911	7.154	0.882	6.871	0.802	6.244	0.622	7.189	0.893	7.068	0.862	7.190	0.894	7.145	0.880
−0.38	7.94	7.301	0.897	7.176	0.867	6.884	0.788	6.250	0.613	7.215	0.879	7.094	0.848	7.216	0.879	7.165	0.865
−0.38	8.91	7.319	0.886	7.192	0.856	6.894	0.776	6.256	0.606	7.234	0.868	7.115	0.837	7.236	0.868	7.178	0.853
−0.38	10.00	7.347	0.877	7.218	0.846	6.912	0.767	6.269	0.601	7.264	0.859	7.145	0.830	7.265	0.859	7.204	0.844
−0.38	11.22	7.350	0.875	7.221	0.844	6.913	0.764	6.274	0.600	7.270	0.857	7.155	0.828	7.271	0.858	7.210	0.843
−0.38	12.59	7.347	0.875	7.217	0.842	6.907	0.761	6.271	0.598	7.270	0.857	7.158	0.828	7.272	0.858	7.210	0.842
−0.38	14.13	7.357	0.872	7.224	0.838	6.906	0.756	6.271	0.594	7.281	0.854	7.170	0.825	7.283	0.855	7.220	0.838
−0.38	15.85	7.382	0.863	7.239	0.828	6.907	0.744	6.266	0.586	7.304	0.845	7.190	0.816	7.306	0.846	7.240	0.829
−0.38	17.78	7.423	0.863	7.276	0.827	6.935	0.743	6.290	0.587	7.346	0.845	7.232	0.817	7.348	0.846	7.280	0.829
0.00	1.00	6.169	1.998	6.024	2.068	5.819	1.951	5.302	1.234	6.031	2.078	5.900	2.062	6.031	2.078	6.029	2.064
0.00	1.12	6.317	1.807	6.188	1.857	5.978	1.746	5.397	1.119	6.196	1.866	6.072	1.846	6.196	1.867	6.192	1.853
0.00	1.26	6.646	1.584	6.531	1.614	6.301	1.522	5.599	1.013	6.541	1.622	6.411	1.604	6.541	1.623	6.534	1.612
0.00	1.41	6.963	1.397	6.857	1.414	6.608	1.336	5.805	0.919	6.869	1.420	6.733	1.403	6.869	1.421	6.859	1.412
0.00	1.58	6.965	1.354	6.867	1.355	6.622	1.263	5.814	0.864	6.881	1.362	6.758	1.332	6.882	1.363	6.870	1.353
0.00	1.78	7.100	1.271	6.998	1.265	6.731	1.171	5.871	0.803	7.014	1.272	6.884	1.237	7.015	1.273	7.000	1.263
0.00	2.00	7.235	1.192	7.124	1.180	6.828	1.086	5.912	0.745	7.144	1.188	7.002	1.152	7.145	1.188	7.126	1.179
0.00	2.24	7.346	1.128	7.231	1.113	6.915	1.020	5.958	0.704	7.253	1.121	7.105	1.084	7.254	1.121	7.233	1.111
0.00	2.51	7.397	1.079	7.281	1.060	6.953	0.967	5.975	0.670	7.306	1.068	7.157	1.030	7.307	1.068	7.282	1.058
0.00	2.82	7.435	1.043	7.320	1.021	6.983	0.928	5.991	0.645	7.347	1.029	7.200	0.990	7.348	1.029	7.321	1.019
0.00	3.16	7.494	1.012	7.375	0.988	7.024	0.895	6.011	0.624	7.406	0.996	7.255	0.957	7.407	0.997	7.376	0.986
0.00	3.55	7.506	0.999	7.386	0.972	7.027	0.878	6.011	0.612	7.420	0.981	7.271	0.942	7.421	0.982	7.387	0.971
0.00	3.98	7.532	0.984	7.408	0.955	7.034	0.858	6.004	0.598	7.445	0.965	7.294	0.924	7.447	0.965	7.408	0.953
0.00	4.47	7.515	0.994	7.390	0.963	7.013	0.862	5.992	0.599	7.430	0.973	7.282	0.931	7.432	0.974	7.391	0.961
0.00	5.01	7.525	0.983	7.399	0.951	7.014	0.849	5.994	0.591	7.442	0.962	7.295	0.919	7.444	0.962	7.399	0.949
0.00	5.62	7.531	0.974	7.402	0.940	7.007	0.836	5.985	0.583	7.449	0.951	7.302	0.909	7.451	0.952	7.402	0.938
0.00	6.31	7.493	0.965	7.355	0.926	6.937	0.816	5.914	0.563	7.408	0.940	7.257	0.895	7.411	0.941	7.355	0.925

Table 3 – *continued*

[M/H]	Age	Unimodal								Bimodal				K. universal		K. revised	
		$\mu = 0.3$		$\mu = 1.3$		$\mu = 2.3$		$\mu = 3.3$		$\mu = 1.3$		$\mu = 2.3$					
	(Gyr)	CaT*	PaT	CaT*	PaT	CaT*	PaT	CaT*	PaT	CaT*	PaT	CaT*	PaT	CaT*	PaT	CaT*	PaT
0.00	7.08	7.481	0.963	7.339	0.922	6.914	0.809	5.898	0.558	7.397	0.937	7.247	0.891	7.400	0.938	7.340	0.920
0.00	7.94	7.467	0.954	7.321	0.912	6.886	0.797	5.876	0.550	7.383	0.928	7.233	0.882	7.386	0.929	7.322	0.910
0.00	8.91	7.465	0.945	7.315	0.902	6.871	0.786	5.867	0.543	7.381	0.919	7.232	0.873	7.385	0.920	7.316	0.900
0.00	10.00	7.459	0.938	7.303	0.893	6.851	0.776	5.852	0.537	7.375	0.911	7.225	0.866	7.379	0.912	7.304	0.891
0.00	11.22	7.431	0.935	7.274	0.890	6.819	0.771	5.836	0.534	7.349	0.909	7.203	0.863	7.353	0.910	7.275	0.887
0.00	12.59	7.413	0.934	7.251	0.887	6.792	0.766	5.820	0.532	7.332	0.907	7.187	0.861	7.335	0.908	7.254	0.884
0.00	14.13	7.390	0.934	7.226	0.885	6.765	0.763	5.808	0.531	7.311	0.907	7.170	0.862	7.315	0.908	7.233	0.884
0.00	15.85	7.364	0.934	7.196	0.884	6.732	0.760	5.789	0.529	7.286	0.907	7.148	0.862	7.290	0.908	7.207	0.884
0.00	17.78	7.335	0.933	7.162	0.881	6.695	0.756	5.768	0.527	7.258	0.906	7.124	0.862	7.263	0.907	7.178	0.882
0.20	1.00	6.677	1.697	6.559	1.746	6.313	1.638	5.484	1.034	6.571	1.755	6.447	1.731	6.571	1.755	6.563	1.743
0.20	1.12	6.812	1.523	6.705	1.556	6.449	1.455	5.564	0.930	6.718	1.564	6.597	1.539	6.719	1.564	6.708	1.553
0.20	1.26	6.981	1.372	6.884	1.393	6.616	1.300	5.667	0.847	6.899	1.400	6.776	1.374	6.899	1.400	6.887	1.390
0.20	1.41	7.350	1.208	7.254	1.220	6.960	1.148	5.904	0.780	7.271	1.226	7.130	1.208	7.271	1.226	7.256	1.218
0.20	1.58	7.262	1.121	7.204	1.124	6.974	1.063	6.011	0.755	7.219	1.128	7.124	1.111	7.219	1.129	7.206	1.123
0.20	1.78	7.531	1.094	7.426	1.089	7.092	1.007	5.963	0.684	7.448	1.095	7.297	1.066	7.449	1.095	7.427	1.087
0.20	2.00	7.619	1.052	7.506	1.041	7.149	0.956	5.982	0.648	7.532	1.048	7.372	1.015	7.533	1.048	7.507	1.040
0.20	2.24	7.685	1.021	7.570	1.004	7.196	0.917	6.004	0.622	7.598	1.011	7.434	0.976	7.599	1.012	7.570	1.003
0.20	2.51	7.717	1.009	7.599	0.987	7.209	0.895	6.001	0.605	7.630	0.995	7.464	0.956	7.631	0.995	7.598	0.986
0.20	2.82	7.744	1.000	7.622	0.974	7.221	0.879	6.001	0.593	7.657	0.982	7.490	0.941	7.658	0.983	7.622	0.973
0.20	3.16	7.751	0.989	7.630	0.961	7.224	0.864	6.008	0.584	7.667	0.969	7.503	0.927	7.669	0.970	7.630	0.960
0.20	3.55	7.717	0.977	7.600	0.948	7.200	0.851	6.003	0.578	7.639	0.957	7.483	0.915	7.640	0.957	7.600	0.947
0.20	3.98	7.680	0.965	7.562	0.934	7.155	0.835	5.968	0.566	7.604	0.943	7.451	0.901	7.606	0.944	7.562	0.933
0.20	4.47	7.664	0.962	7.545	0.930	7.132	0.829	5.954	0.563	7.589	0.940	7.438	0.897	7.591	0.941	7.545	0.929
0.20	5.01	7.627	0.966	7.504	0.931	7.081	0.826	5.911	0.558	7.552	0.943	7.401	0.899	7.554	0.943	7.504	0.930
0.20	5.62	7.612	0.957	7.485	0.921	7.052	0.814	5.886	0.549	7.537	0.933	7.386	0.889	7.540	0.934	7.486	0.920
0.20	6.31	7.590	0.948	7.456	0.910	7.007	0.799	5.843	0.537	7.514	0.923	7.361	0.878	7.517	0.924	7.457	0.908
0.20	7.08	7.570	0.930	7.430	0.891	6.967	0.780	5.809	0.524	7.492	0.905	7.338	0.861	7.495	0.906	7.431	0.890
0.20	7.94	7.516	0.860	7.375	0.826	6.912	0.727	5.774	0.495	7.441	0.840	7.291	0.804	7.444	0.841	7.378	0.826
0.20	8.91	7.524	0.866	7.374	0.830	6.893	0.726	5.755	0.492	7.446	0.845	7.292	0.807	7.449	0.846	7.377	0.829
0.20	10.00	7.536	0.896	7.375	0.855	6.878	0.742	5.738	0.499	7.454	0.872	7.295	0.830	7.457	0.873	7.378	0.854
0.20	11.22	7.519	0.883	7.353	0.842	6.849	0.729	5.721	0.492	7.436	0.860	7.278	0.819	7.440	0.861	7.357	0.841
0.20	12.59	7.484	0.877	7.313	0.835	6.803	0.721	5.692	0.487	7.402	0.854	7.246	0.814	7.406	0.856	7.318	0.834
0.20	14.13	7.450	0.864	7.274	0.822	6.757	0.708	5.662	0.479	7.369	0.842	7.214	0.803	7.373	0.843	7.283	0.822
0.20	15.85	7.399	0.861	7.218	0.817	6.698	0.701	5.625	0.474	7.319	0.839	7.167	0.800	7.324	0.840	7.232	0.818
0.20	17.78	7.346	0.855	7.160	0.809	6.636	0.691	5.584	0.468	7.267	0.833	7.119	0.794	7.272	0.834	7.179	0.811

given set of stellar atmospheric parameters, a representative average spectrum and index value, respectively. One of the main differences between these two methods is that the spectral synthesis works at much higher resolution in the stellar parameter space than that used for calculating the fitting functions. In the boxes method employed in the spectral synthesis those stars for which the parameters more closely resemble the requested ones are assigned significantly larger weights when computing a representative spectrum (see Appendix B). Therefore, since the spectral synthesis emphasizes the contribution of the most likely stars, the obtained differences between the two sets of model predictions are expected to be larger when a given set of stars, with a relevant contribution within a stellar population, is lacking. In fact, the lack of giant stars of temperatures lower than ∼4200 K (see Fig. 2) causes the main differences seen for [M/H] = −0.38 and −0.68. However, for [M/H] < −1.0 these differences are smaller because the coolest stars along the isochrones have larger temperatures than those for more metal-rich stellar populations and, therefore, the lack of these stars constitutes a less severe problem. However, we note that these differences in the predictions of the two model approaches are of the order of typical observational errors in galaxy spectra (see Paper I and C03). Moreover, these differences are considerably smaller than those obtained from comparisons between different author predictions (see Section 7).

It is worth noting that the SSP spectra obtained for [M/H] = −1.28 and −1.68 are less reliable than those for higher metallicities owing to the lack, in our stellar library, of spectra representing important evolutionary phases. In particular, this is the case for stars corresponding to the MS turn-off (i.e. dwarfs with temperatures larger than 6000 K), or the blue horizontal branch, which is more prominent for SSPs of ages above 13 Gyr (see Fig. 2). This is the reason why in Fig. 5 we only show the CaT* values measured in the spectra corresponding to SSPs for ages in the range 10–13 Gyr, where the contribution of these stars is smaller.

Fig. 6 shows the effects of the metallicity (top panels), age (middle) and IMF (bottom) on the synthesized SSP spectra at a resolution of $\sigma = 200$ km s^{-1} (left-hand panels) and $\sigma = 22.2$ km s^{-1} (right-hand panels). We overplot in the upper panels various representative SSP spectra of similar age (i.e. 10 Gyr) and IMF (unimodal, $\mu = 1.3$), and with different metallicities. We have chosen to normalize all the spectra to the continuum at λλ8619–8642 (see Table 1), to be able to see the effect of the metallicity on the third line of the Ca II triplet feature, which can be taken as representative of the overall Ca II triplet feature. We see that the depth of this line is

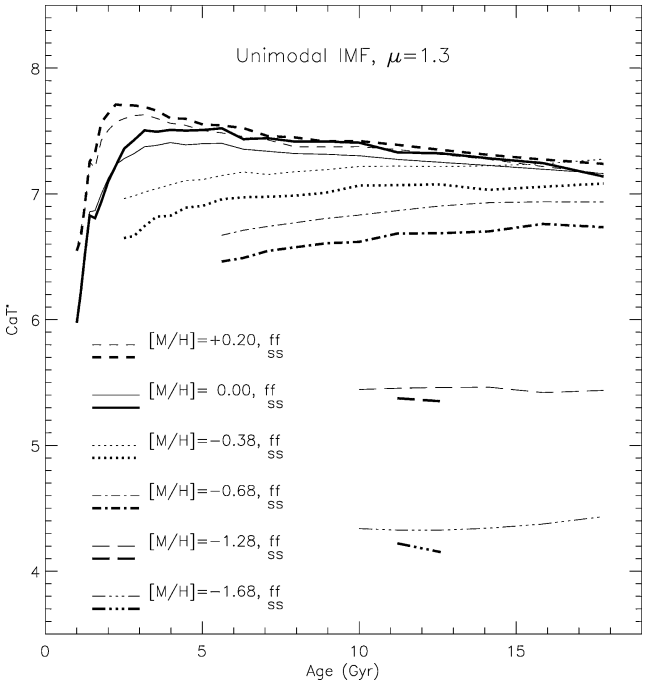

Figure 5. The CaT* index in SSPs as a function of age and metallicity. Different line types refer to the metallicity of the SSP, as quoted in the plot. All the models are calculated with a unimodal IMF of slope $\mu = 1.3$. We plot the CaT* index as calculated on the basis of the fittings functions of Paper III (ff, thin lines), and as measured on the synthesized spectra (ss, thick lines). The spectral resolution is 1.5 Å (FWHM) (i.e. $\sigma = 22.2$ km s^{-1}) for the two set of predictions.

virtually constant in the metallicity range (i.e. $-0.7 <$ [M/H] < 0.2). We obtain similar results for the other lines if normalizing to the appropriate continua. We note, however, a strong variation of the slope of the continuum around the Ca II triplet feature. For a given age and IMF, the larger the metallicity the larger the slope of this continuum. The overall shape of the continuum for SSPs of high metallicities shows strong similarities to those of early M-type stars. In this spectral range the contribution of these cool stars to the total luminosity is significantly larger (see Fig. 4) than in the visible, where the integrated spectra resemble those of K-giants. The slope of these spectra and its comparison with galaxy spectra are discussed in C03.

The effect of the age on SSP spectra of the same metallicity (i.e. solar) and IMF (unimodal with slope 1.3) is shown in the second row of panels of Fig. 6, where we vary the SSP age from 2.0 to 17.8 Gyr. We do not see any significant variation either on the Ca II triplet feature or on the overall shape of the spectrum.

4.2 The effects of the IMF

The third row of panels in Fig. 6 illustrates the effect of the IMF on the SSP spectra. In these plots we keep the age (10 Gyr) and the metallicity (solar) constant and vary the slope of the IMF from $\mu = 0.3$ to 3.3. We see that the third line of the Ca II triplet feature is not significantly affected when the slope of the IMF varies from $\mu = 0.3$ to $\sim$2.0, but the line rapidly weakens for extremely dwarf-dominated IMFs. This result is quantified in Fig. 7, where we show the CaT* index for different IMF types and slopes. The top panels show the values obtained for different slopes and a unimodal IMF. The larger the metallicity is the larger the weakening of the CaT* index as a function of increasing the IMF slope. This effect is not remarkable for lower metallicities, although we do see an opposite trend for metallicities below [M/H] < -1.0. Fig. 4 shows the reason for this behaviour: the larger the IMF slope is the larger the relative contribution of the MS stars (with lower Ca II triplet strengths, see Paper III) to the total luminosity and to the contribution of the RGB phase (see from top to bottom panels).

In the two bottom panels of Fig. 7 starting from the left we show the results for a bimodal IMF for two different slopes, i.e. $\mu = 1.3$ and 2.3. These plots show that the effect of the IMF slope on the CaT* index is much less pronounced for this IMF. This result is expected since for the bimodal IMF the contribution of the very low MS stars is decreased with respect to a unimodal IMF of the same slope. Finally, in the last two panels we plot the results for the universal and revised IMF of K01. This figure and the index values tabulated in Table 3 indicate that the CaT* values obtained from the unimodal and bimodal IMFs of slope $\mu = 1.3$ and the two IMFs of K01 are very similar. However, the CaT* values obtained with the universal IMF more closely match those of the bimodal IMF, whilst those of the revised IMF match those of the unimodal shape. This result is easily understood by looking at Fig. 1.

5 CA II TRIPLET FEATURE DEPENDENCE ON SPECTRAL RESOLUTION

In order to study the sensitivity of the Ca II triplet indices to the spectral resolution, or galaxy velocity dispersion broadening (σ), we have broadened the whole SSP model spectral library by convolving with Gaussians from $\sigma = 25$ km s^{-1} up to $\sigma = 400$ km s^{-1} (in steps of 25 km s^{-1}). The Ca II triplet indices were measured for the full set of broadened spectra and we fit, for each model, a third-order polynomial to the relative changes of the index values as a function of velocity dispersion

$$\frac{\mathcal{I}(\sigma) - \mathcal{I}(\sigma_0)}{\mathcal{I}(\sigma)} = a + b\sigma + c\sigma^2 + d\sigma^3 \equiv p(\sigma), \quad (8)$$

where $\sigma_0 = 22.2$ km s^{-1} is the nominal resolution of the models (FWHM = 1.50 Å). Finally, making use of this formula it is straightforward to relate the indices measured at two different velocity dispersions, σ_1 and σ_2.

Table 4 tabulates the derived coefficients for the CaT* and CaT indices measured over a number of representative SSP models. The velocity dispersion corrections for the PaT index can be inferred from those of the CaT* and CaT indices. We plot in Fig. 8 the obtained ΔCaT*/CaT* and ΔCaT/CaT values for this set of representative models. The grey region represents the locus of broadening corrections for the whole SSP model spectral library. Note that the CaT index is significantly more sensitive to the velocity dispersion than the CaT* index. This result is in agreement with that obtained in Paper I for stars. In that paper, it was shown that PaT is quite sensitive to velocity dispersion broadening. The improvement in the CaT* sensitivity is explained since the effects of the broadening on CaT and PaT indices are partially compensated when the CaT* index is computed. Paper I also shows that the CaT* index is less sensitive to resolution than most of the other popular index definitions for this feature.

The fact that the broadening correction depends on the model parameters shows us to what extent one can match the effects of galaxy velocity broadening using a number of stellar templates. In fact, the stellar spectra show even larger variations than those shown by the models (as it can be seen by comparing Fig 8 with 5a of Paper I). Note that this method has been widely used in the literature to also match the resolution requirements of the Lick/IDS system of

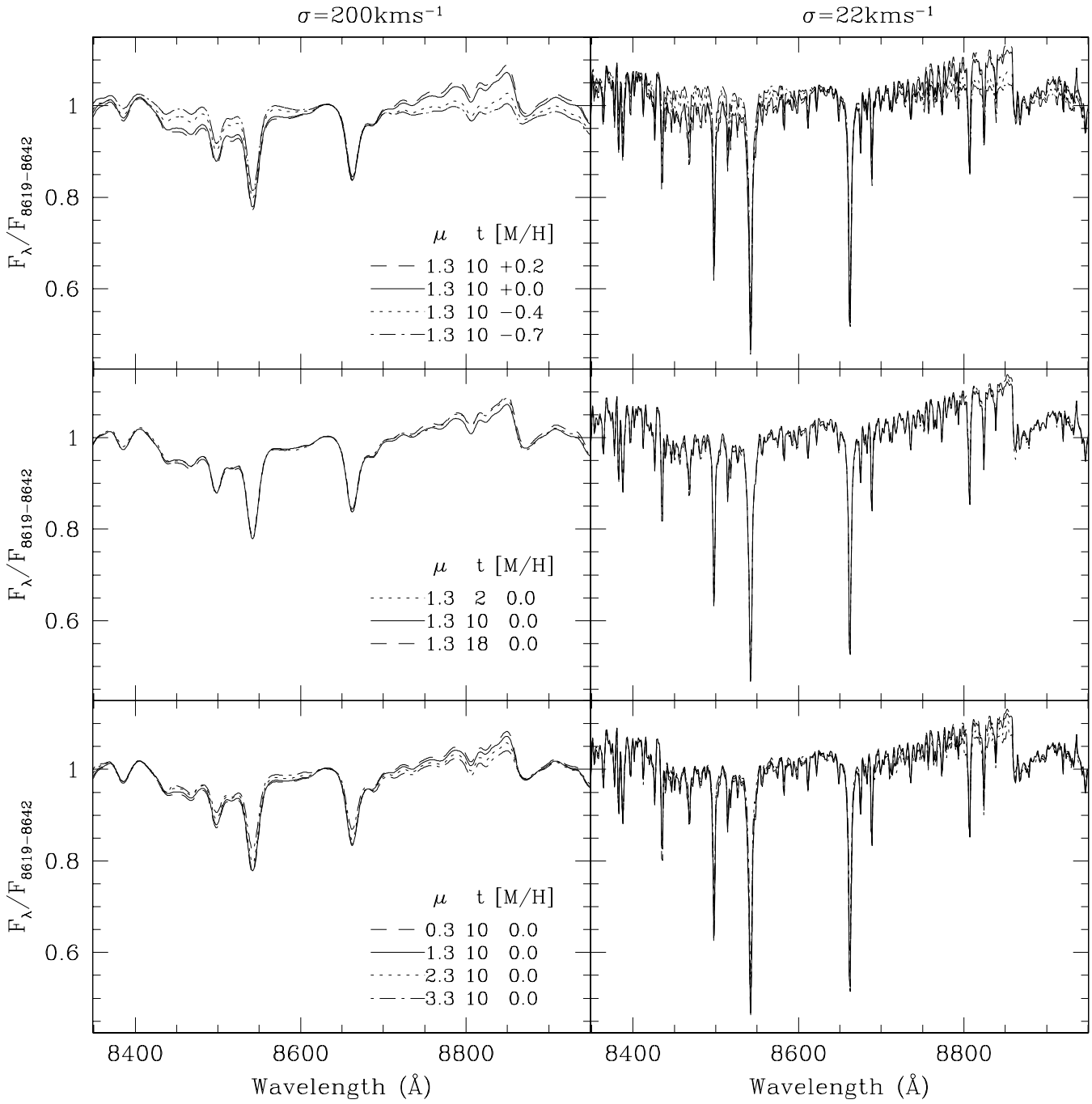

Figure 6. Model SSP spectra at $\sigma = 200$ and 22.2 km s^{-1} (i.e. the nominal resolution) for SSPs of different metallicities (upper plot), ages (middle) and IMF slopes (bottom). The models were calculated using a unimodal IMF. All the spectra were normalized by the flux in the range λλ8619–8642.

indices in the optical spectral range in order to compare galaxy line-strength measurements with the index predictions of models based on that system (Worthey 1994; V96). The reader is referred to the extensive review of WO97 for a detailed description of the method. It is evident that the method that we propose here to smooth the new model spectra to galaxy velocity dispersion (and resolution of the data) does not suffer from these broadening correction uncertainties. The advantages of this approach over the traditional method, based on the stellar templates, has also been proven by Falcón-Barroso et al. (2003), who have used the new SSP models presented here as templates for deriving accurate stellar velocities, velocity dispersions and higher-order Gauss–Hermite moment profiles.

It is interesting to see whether the information provided by the CaT* index, in terms of the relevant parameters of the stellar populations, varies as a function of galaxy velocity dispersion. For this purpose we plot in Fig. 9 the CaT* index measured on the model SSP spectral library smoothed from $\sigma = 50$ to 300 km s^{-1}. We see some relative variations between the model lines of different metallicities, e.g. the separation between the lines corresponding to [M/H] $= -0.68$ and $= +0.2$ is larger at $\sigma = 300$ km s^{-1} than at

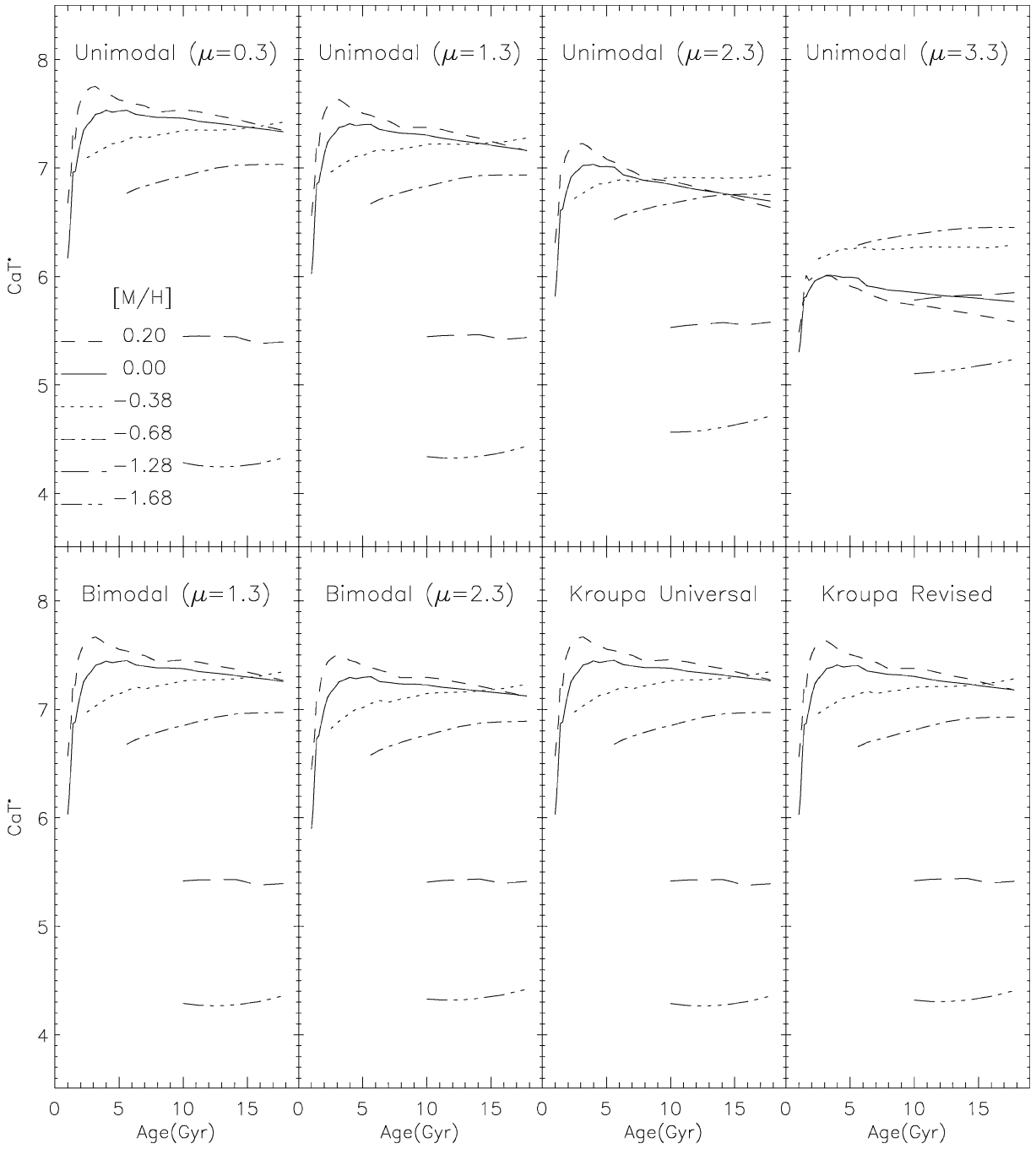

Figure 7. The CaT* index as a function of the IMF. All the models shown here are calculated on the basis of the fitting functions.

$\sigma = 50\,\mathrm{km\,s^{-1}}$. However, these differences are small in comparison with typical observational errors (see Paper I and C03) and, therefore, the stellar population parameter estimates obtained on the basis of this index do not depend significantly on the adopted resolution.

6 SOLAR METALLICITY MODELS IN THE AGE INTERVAL 0.1–1 GYR

Although the predictions for young stellar populations will be described in detail in a forthcoming paper, in this section we extend the age of our SSP models down to 0.1 Gyr for solar metallicity. When compared with old stellar populations there are several major changes in the relative contributions to the total luminosity of the different evolutionary stages in this age range. In fact, the MS, HB and AGB phases increase their contributions, whilst the RGB mostly disappears. In Fig. 10 we plot a set of representative SSP spectra corresponding to 0.2 and 2 Gyr for solar metallicity and unimodal IMF of slope 1.3 (for two different spectral resolutions). As was expected, there is a significant strengthening of the Paschen series towards younger ages (see, for example, the change in the strength of the lines at either side of the third Ca II triplet line). This result is a consequence of the increased contribution of hotter MS stars to the total luminosity in this spectral range. We also see that the continuum around the Ca II triplet feature is significantly affected by

Table 4. Coefficients of the broadening correction polynomials $\Delta\mathcal{I}/\mathcal{I} = a + b\sigma + c\sigma^2 + d\sigma^3$) for the CaT* and CaT indices for a set of representative SSP models (μ, [M/H], t).

$\mathcal{I}$	Model	$a(\times10^{-3})$	$b(\times10^{-5})$	$c(\times10^{-7})$	$d(\times10^{-9})$
CaT*	1.3, 0.0, 1.0	−2.058 826	8.056 297	6.404 771	−4.142 633
	1.3, 0.0, 12.6	−3.987 821	16.893 273	5.690 300	−3.923 405
	1.3, −0.7, 12.6	−3.632 453	15.659 963	4.025 051	−3.878 037
	2.8, 0.0, 1.0	−2.989 543	12.448 730	5.462 115	−3.954 834
	2.8, 0.0, 12.6	−4.815 550	20.660 642	5.485 660	−3.790 087
	2.8, −0.7, 12.6	−4.428 785	19.288 911	3.811 699	−3.766 459
CaT	1.3, 0.0, 1.0	−2.958 673	15.256 039	−7.750 521	−4.221 853
	1.3, 0.0, 12.6	−6.121 178	29.992 397	−0.101 206	−3.505 068
	1.3, −0.7, 12.6	−4.687 171	23.040 400	−7.787 181	−4.022 836
	2.8, 0.0, 1.0	−3.215 187	16.386 110	−7.673 347	−4.054 138
	2.8, 0.0, 12.6	−6.122 020	29.828 926	−9.389 365	−3.405 152
	2.8, −0.7, 12.6	−5.524 840	27.065 372	−8.985 443	−3.732 187

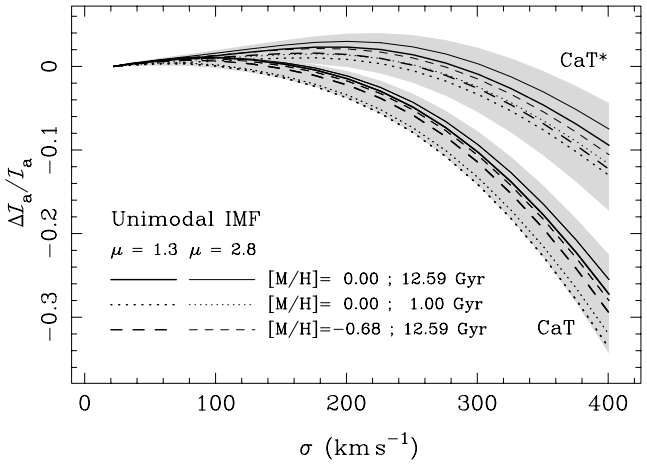

Figure 8. Broadening correction ΔCaT*/CaT* and ΔCaT/CaT for the Ca II triplet feature in SSPs. To calculate these corrections we have broadened the model spectra by convolving with Gaussians from $\sigma = 25$ km s^{-1} up to $\sigma = 400$ km s^{-1} in steps of 25 km s^{-1}. $\Delta I/I$ is zero for $\sigma = 22.2$ km s^{-1} (the spectral resolution of the stellar library). We plot with different line types the broadening corrections for a set of representative models of different ages (1, 12.59 Gyr), metallicities (0.0, −0.68) and IMFs (unimodal, $\mu = 1.3$, $\mu = 2.8$). In grey we show the region covered by the broadening corrections obtained for the whole model SSP spectral library. The upper envelope for the two indices corresponds to the model $\mu = 3.3$, [M/H] = +0.2 and 17.78 Gyr, whereas the lower envelope refers to the model $\mu = 0.3$, [M/H] = −1.3 and 14.12 Gyr.

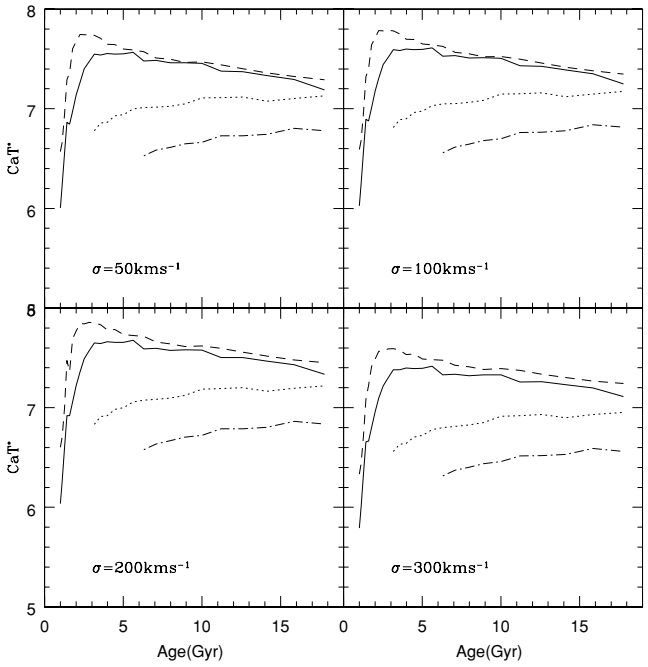

Figure 9. The CaT* index measured on the model SSP spectral library smoothed to $\sigma = 50$, 100, 200 and 300 km s^{-1}. We use a unimodal IMF of slope 1.3.

the molecular band absorptions, which constitute a typical feature of the M-type stars. This continuum shape with its characteristic slope is attributed to the contribution of the AGB phase (see Appendix C), whilst similar shapes are obtained for older stellar populations owing to the contribution of the RGB.

In Fig. 11 we show the time evolution of the PaT, CaT* and CaT indices. The plot shows the strengthening of the PaT index and the weakening of the CaT* index towards younger SSPs. Interestingly, these changes are compensated in a such a way that the CaT index is virtually constant in this age range, and have similar values to those obtained for older stellar populations. Finally, it is worth noting that the Paschen series cannot be detected for SSPs of ages greater than ∼1.5 Gyr. In Table 5 we list the predicted CaT* and PaT index values corresponding to this age interval for several IMF types.

7 COMPARISON WITH PREVIOUS PREDICTIONS

In Fig. 12 we compare our CaT index predictions (which superseed those of V96) with those of MGV (which superseed those of García-Vargas et al. 1998) and ITD. These authors employ different Ca II triplet index definitions (see Paper I for an extensive comparison between different systems). However, we can transform their predictions to our system on the basis of the relations given in table 8 of Paper I. In that paper we presented two sets of calibrations to convert between different systems. The first set accounted for the effect of different Ca II triplet index definitions, while the second set can be used to correct for flux calibration effects and differences in spectral resolution. The composite calibrations to convert the predictions of MGV, CaT(MGV), which are on the system by Díaz et al. (1989) and ITD, CaT(ITD), which employ the system by AZ88, to our CaT

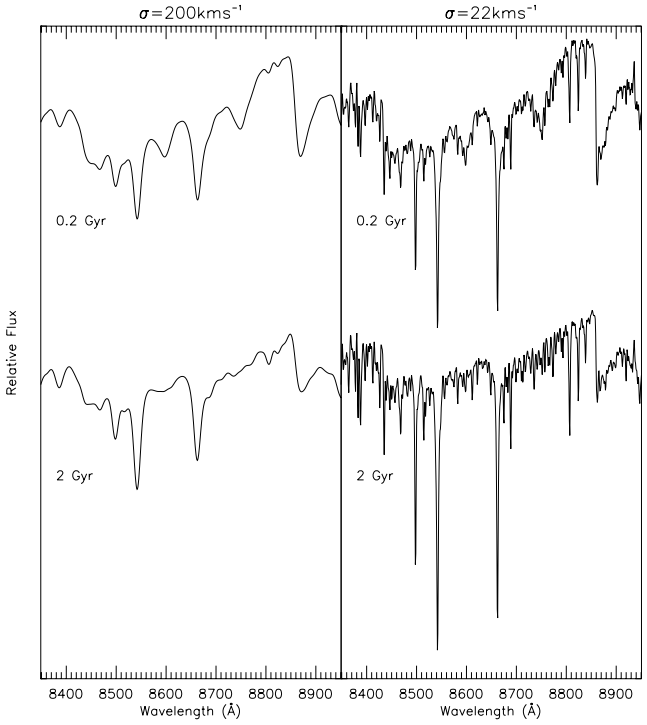

Figure 10. From top to bottom: SSP model spectra of 0.2 and 2.0 Gyr for solar metallicity and unimodal IMF with slope 1.3. The left-hand panel spectra were smoothed to $\sigma = 200$ km s^{-1}, whilst the right-hand panel spectra are kept at the nominal resolution of the models, i.e. $\sigma = 22.2$ km s^{-1}.

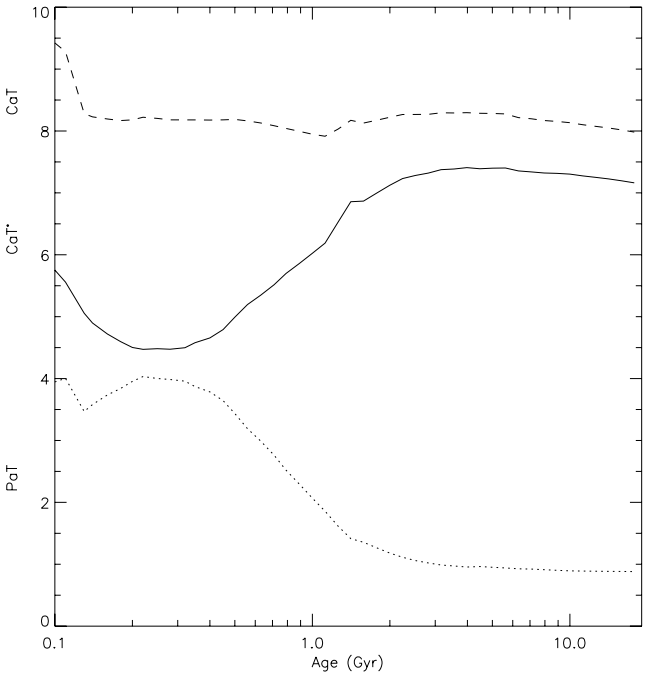

Figure 11. Time evolution of the CaT (dashed line), CaT* (solid line) and PaT (dotted line) indices for intermediate aged SSPs. These predictions are calculated on the basis of a unimodal IMF of slope 1.3 and solar metallicity. The spectral resolution is 1.5 Å (FWHM).

Table 5. Predicted CaT* and PaT indices for intermediate-age SSPs for solar metallicity and different IMF shapes (for the unimodal and bimodal IMFs we adopt $\mu = 1.3$). The tabulated index values are calculated on the basis of the empirical fitting functions given in Paper III. The spectral resolution is 1.5 Å (FWHM). The CaT index can be obtained from the relation CaT = CaT* + 0.93 PaT.

Age	Unimodal		Bimodal		K. universal		K. revised	
(Gyr)	CaT*	PaT	CaT*	PaT	CaT*	PaT	CaT*	PaT
0.10	5.753	3.946	5.755	3.952	5.755	3.953	5.755	3.942
0.11	5.558	4.003	5.560	4.010	5.560	4.010	5.561	3.999
0.13	5.055	3.468	5.056	3.473	5.056	3.473	5.057	3.466
0.14	4.898	3.580	4.899	3.586	4.898	3.586	4.901	3.578
0.16	4.720	3.735	4.720	3.741	4.720	3.742	4.723	3.732
0.18	4.597	3.840	4.596	3.847	4.596	3.848	4.600	3.836
0.20	4.502	3.954	4.502	3.963	4.502	3.963	4.507	3.950
0.22	4.472	4.033	4.471	4.042	4.471	4.043	4.477	4.028
0.25	4.483	4.001	4.482	4.011	4.482	4.011	4.488	3.996
0.28	4.474	3.985	4.473	3.995	4.473	3.996	4.479	3.979
0.32	4.498	3.958	4.497	3.969	4.497	3.970	4.504	3.952
0.35	4.579	3.871	4.578	3.882	4.578	3.883	4.585	3.865
0.40	4.657	3.784	4.656	3.796	4.656	3.797	4.662	3.778
0.45	4.791	3.644	4.791	3.657	4.791	3.658	4.797	3.638
0.50	4.992	3.435	4.993	3.447	4.993	3.448	4.998	3.429
0.56	5.196	3.190	5.198	3.202	5.198	3.203	5.202	3.184
0.63	5.347	2.990	5.350	3.002	5.350	3.003	5.353	2.985
0.71	5.516	2.762	5.520	2.774	5.520	2.775	5.522	2.757
0.79	5.698	2.520	5.703	2.531	5.703	2.531	5.704	2.515
0.89	5.859	2.295	5.865	2.305	5.865	2.306	5.865	2.290
1.00	6.024	2.068	6.031	2.078	6.031	2.078	6.029	2.064

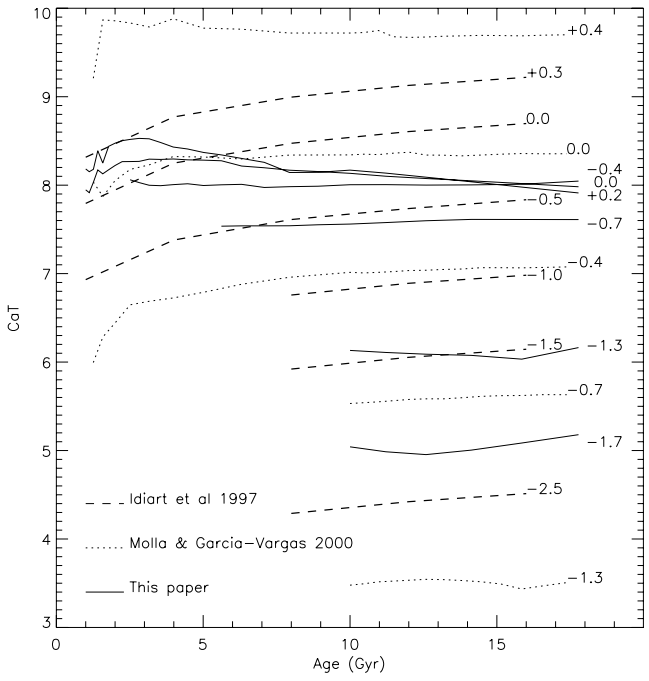

Figure 12. Comparison of the CaT index predictions by different authors for SSPs of different metallicities and ages. All the models are calculated with a Salpeter IMF. The dotted lines refer to the predictions of MGV, the dashed lines refer to ITD and the solid line represents our predictions. To perform this comparison we have transformed their predictions to our system on the basis of the formulae given in Paper I (see the text).

index are the following:

$$\begin{aligned} \mathrm{CaT} &= 0.533 + 1.103\mathrm{CaT(MGV)} \\ \mathrm{CaT} &= -0.155 + 1.183\mathrm{CaT(ITD)}. \end{aligned} \quad (9)$$

In Fig. 12 we compare the tabulated predictions of these authors (converted to our system) with ours. Among the main differences, we must remark that their CaT index predictions increase as a function of metallicity for all metallicity regimes, whilst we obtain a saturation of this index for metallicities above ~ -0.5. This saturation can be explained in part by the fact that the larger the metallicity the lower is the difference between the contributions of the main sequence (lower CaT values) and the red giant branch (larger CaT values) to the total luminosity of an SSP, as can be seen in Fig. 4 (second row of panels, i.e. $\mu = 1.3$). Moreover, in metal-rich SSPs the RGB is populated with an increasing fraction of cold stars, and, for temperatures cooler than ~3750 K, the CaT index decreases dramatically with decreasing temperature (see fig. 7 of Paper III). The main point is that this behaviour for the M giants is not predicted by the fitting functions used by these authors since their stellar libraries do not include these stars.

In the case of ITD, the coolest stars included in their library are of K3 spectral type. MGV extrapolate to lower temperatures the theoretical fitting functions of Jørgensen et al. (1992), valid only for $T_{\rm eff} \geqslant 4000$ K. Note that although MGV try to justify this extrapolation in their fig. 1, their argument is not completely correct. For instance, for a giant star of $T_{\rm eff} = 3000$ K (which has a gravity of $\log g \sim 0$), the Jørgensen et al. extrapolated fitting functions predict CaT = 9.84 Å (11.39 Å when corrected to our system), whereas the actual CaT measured values in our library stars of similar parameters range from 2.3 to 5.0 Å.

These effects may also explain the fact that these authors obtain slightly larger CaT values for increasing ages, whilst our predictions for the time evolution of the CaT index is towards slightly lower values for SSPs of large metallicities.

For lower metallicities, our CaT predictions are in better agreement with the predictions of ITD, whilst those of MGV show much lower values. This can be explained on the basis of fig. 12 of Paper III, where it can be seen that the fitting functions of Jørgensen et al. predict a larger dependence on metallicity than what is actually observed.

The first paper on synthesizing SSP spectra at high resolution in this spectral range is that of SBB. These authors follow a completely different approach than that used in this paper. They employ a fully synthetic stellar spectral library calculated by Schiavon & Barbuy (1999), which is based on model photospheres and molecular and atomic line lists. Another important difference is that they adopt the old Padova set of isochrones (B94), whilst we make use of the new Padova set. Fig. 13 shows a comparison of a representative SSP model spectrum, kindly provided to us by these authors, to an equivalent spectrum of our model library. These spectra correspond to a Salpeter IMF, solar metallicity and 13 Gyr and have a resolution 2 Å (FWHM). They were normalized according to the flux in the spectral range covered by our models. In the lower panel of Fig. 13 we plot the difference between these two models. Although we see some differences in the pseudocontinua, particularly in the bluest one, the main difference is in the depth of the Ca II triplet feature. We have measured the CaT index of the SBB spectra and find that their Ca II triplet strengths are 2.5–3 Å lower than the values we obtain for the SSP spectra of our model library. In particular, for the spectra plotted in Fig. 13 we obtain 4.25 Å for the SBB spectrum and 7.33 Å for our spectrum. Schiavon (private communication) suggests that the difference in the Ca II triplet strength can be attributed in part to the fact that their synthetic stellar spectral library was calculated without adopting a non-local thermal equilibrium approach, which it is needed to properly model the depth of the lines. In fact, we have compared the empirical stellar spectra of our library with synthetic stellar spectra of similar atmospheric parameters of their model grid and found that their Ca II triplet values are systematically lower for the giant stars. These differences may be as high as 5 Å. On the other hand, we find a reasonably good agreement for dwarf stars. This comparison shows that further work on the theoretical libraries, including appropriate input physics and updated opacities, is required for this spectral range in order to be able to make use of these libraries for stellar population synthesis modelling.

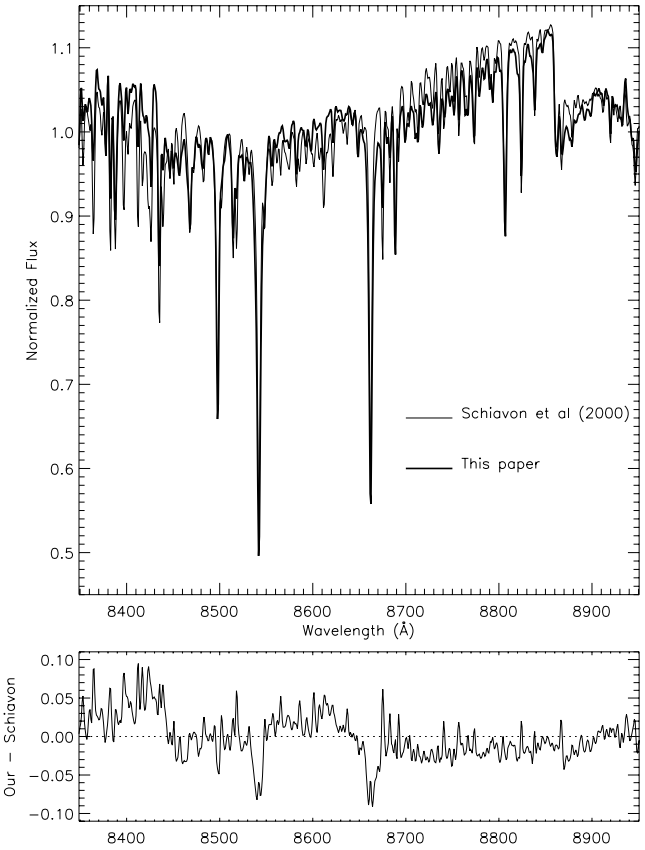

Figure 13. Normalized representative SSP model spectra of SBB (thin line) and this work (thick line). The two models have a Salpeter IMF, solar metallicity and 13 Gyr. The spectra were smoothed to FWHM = 2 Å. The difference between these two spectra is shown in the lower panel.

8 COMPARISON WITH GLOBULAR CLUSTERS AND EARLY-TYPE GALAXIES

8.1 Globular clusters

Globular clusters are the ideal candidates for checking our model predictions since they can be treated as single-age, single-metallicity, stellar populations. We follow here the test suggested by ITD to calibrate our Ca II triplet predictions versus the semi-empirical metallicity calibration of AZ88. For this purpose, we need to transform their galactic globular cluster Ca II triplet index measurements (i.e. $\sum W$, following the notation of these authors) to

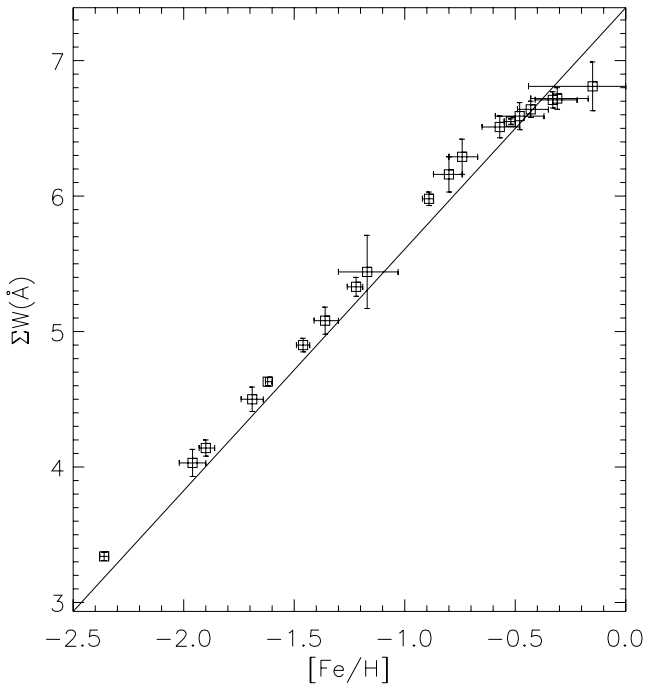

Figure 14. Galactic globular cluster Ca II triplet index measurements given by AZ88 (i.e. $\sum W$) versus the metallicities predicted by our models, when transforming from their system to ours, by means of the CaT index. We assumed a Salpeter IMF and that the clusters are 14 Gyr old (see the text). For clusters with [Fe/H] < -1.68 we extrapolated our model predictions. The solid line represents the AZ88 calibration.

our system by means of the CaT index. This conversion is required since these authors used a different spectral resolution and dispersion and did not correct their data to a relative flux scale. Therefore, we first applied the broadening correction given in table 7 of Paper I to translate their measurements, i.e. at a resolution of 4.8 Å, to ours (1.5 Å). The second step is to transform their $\sum W$ index (on their instrumental response curve) to our CaT index (on a relative flux scale) by making use of equation (9).

The fact that our models show that the Ca II triplet feature exhibits a negligible dependence on the age of the stellar population, for the age range that is usually assumed for the globular clusters, makes it possible to neglect this parameter. Fig. 14 shows our metallicity estimates obtained from a comparison of the corrected CaT measurements with our predictions for models of 14 Gyr and unimodal IMF of slope 1.3. We note that we extrapolate the models for [Fe/H] < -1.68. The solid line represents the AZ88 calibration $[\mathrm{Fe/H}]_{\mathrm{Ca\,II}} = -4.146 + 0.561 \sum W$). Fig. 14 shows the good agreement achieved for metallicities smaller than ~ -0.5. This result probes the validity of using the Ca II triplet of integrated spectra as an alternative method to derive metallicities in globular clusters of [M/H] < -0.5.

Fig. 14 also shows a small shift between the obtained metallicities Δ[Fe/H] < 0.15 dex. In part, this shift may be explained by the large sensitivity of the $\sum W$ index of AZ88 to the spectral resolution, as was shown in Paper I. In fact, we have tested that for a resolution mismatch of $\sim$20 km s^{-1} the obtained offset vanishes. This mismatch could either be originated if the AZ88 resolution differs from 4.8 Å (these authors obtained their observations in different telescopes and used different instrumental setups) or by our assumption of taking the broadening correction representing an M0 star, according to Paper I. An important factor to be taken into account to explain the obtained metallicity shift is the fact that we adopted the Carretta & Gratton (1997) scale for the cluster stars of our stellar spectral library (see Paper II). Moreover, for the stars of M71 we adopted here an even lower metallicity value (i.e. [Fe/H] $= -0.84$) than that predicted by Carretta & Gratton (1997) (i.e. [Fe/H] $= -0.70$), as discussed in Section 3.1.1. It has been largely discussed in the literature that this scale, based on high-dispersion spectra, shows significant deviations from the Zinn & West (1984) scale, which was adopted by AZ88. This effect is more pronounced for the largest metallicities. We refer the reader to the discussion presented in Rutledge et al. (1997).

Finally, we note that for metallicities larger than ~ -0.5 the measured CaT index does not increase as a function of metallicity, departing from the metallicity scale relation of AZ88. Therefore, these measurements are in agreement with our model predictions. However, as a result of this saturation, we are not able to provide accurate metallicity estimates for the most metal-rich globular clusters on the basis of the Ca II triplet.

8.2 Early-type galaxies

In C03 we have applied these models to a large sample of early-type galaxies of different luminosities. In that paper we analyse the Ca II triplet as well as newly defined features, such as the slope of the continuum around the Ca II triplet lines and the Mg I feature at 8807 Å. We therefore refer the reader to that paper for a complete description of the galaxy sample and for an extensive discussion of their stellar populations. In this section, we aim to show the potential use of the new models by selecting two representative galaxies from the C03 sample that have already been analysed in the blue spectral range (V01A) on the basis of very high-quality spectra that allowed us to measure the new age indicator $\mathrm{H}\gamma_\sigma$ of VA99, which does not depend on metallicity. These galaxies are NGC 4478 and 4365. The galaxy spectra that we use here correspond to the central 4-arcsec aperture.

The synthesized model spectra both in the blue (V99) and in the spectral region of the Ca II triplet can be used to analyse the observed galaxy spectra in a very easy and flexible way, allowing us to adapt the theoretical predictions to the characteristics of the data, instead of proceeding in the opposite direction as, for example, we must do when we have to compare our data with models based on the widely used Lick/IDS system (see V99 for an extensive discussion of the advantages of the new approach). After smoothing the synthetic SSP spectra, with flux-calibrated spectral response curves, to the measured resolution (i.e. $\sigma^2_{\mathrm{total}} = \sigma^2_{\mathrm{galaxy}} + \sigma^2_{\mathrm{instr}}$), we can analyse the galaxy spectrum in its own system. The spectral resolution of the near-IR spectra that we use here is $\sigma_{\mathrm{instr}} = 42$ km s^{-1}. We then measure our favourite spectral features, such as the Ca II triplet, in both the models and the data in order to build up index–index diagrams that can help us to obtain the most relevant stellar population parameters.

In Fig. 15 we combine our new Ca II triplet index measurements (C03) with the blue index measurements of V01A. The CaT* and CaT indices are plotted versus the $\mathrm{H}\gamma_{100<\sigma<175}$ and $\mathrm{H}\gamma_{225<\sigma<300}$ indices of VA99. Each $\mathrm{H}\gamma_\sigma$ index definition provides stable and sensitive age predictions within the σ ranges quoted in the subindices. Therefore, whereas the first index is that appropriate for studying NGC 4478 (i.e. $\sigma_{\mathrm{total}} = 140$ km s^{-1}), the second is adequate for studying NGC 4365 (i.e. $\sigma_{\mathrm{total}} = 260$ km s^{-1}). The metallicity of the models increases from the left- to the right-hand panels as quoted above the top panels. We use models of unimodal IMF characterized by its slope μ, which is constant along the vertical solid lines.

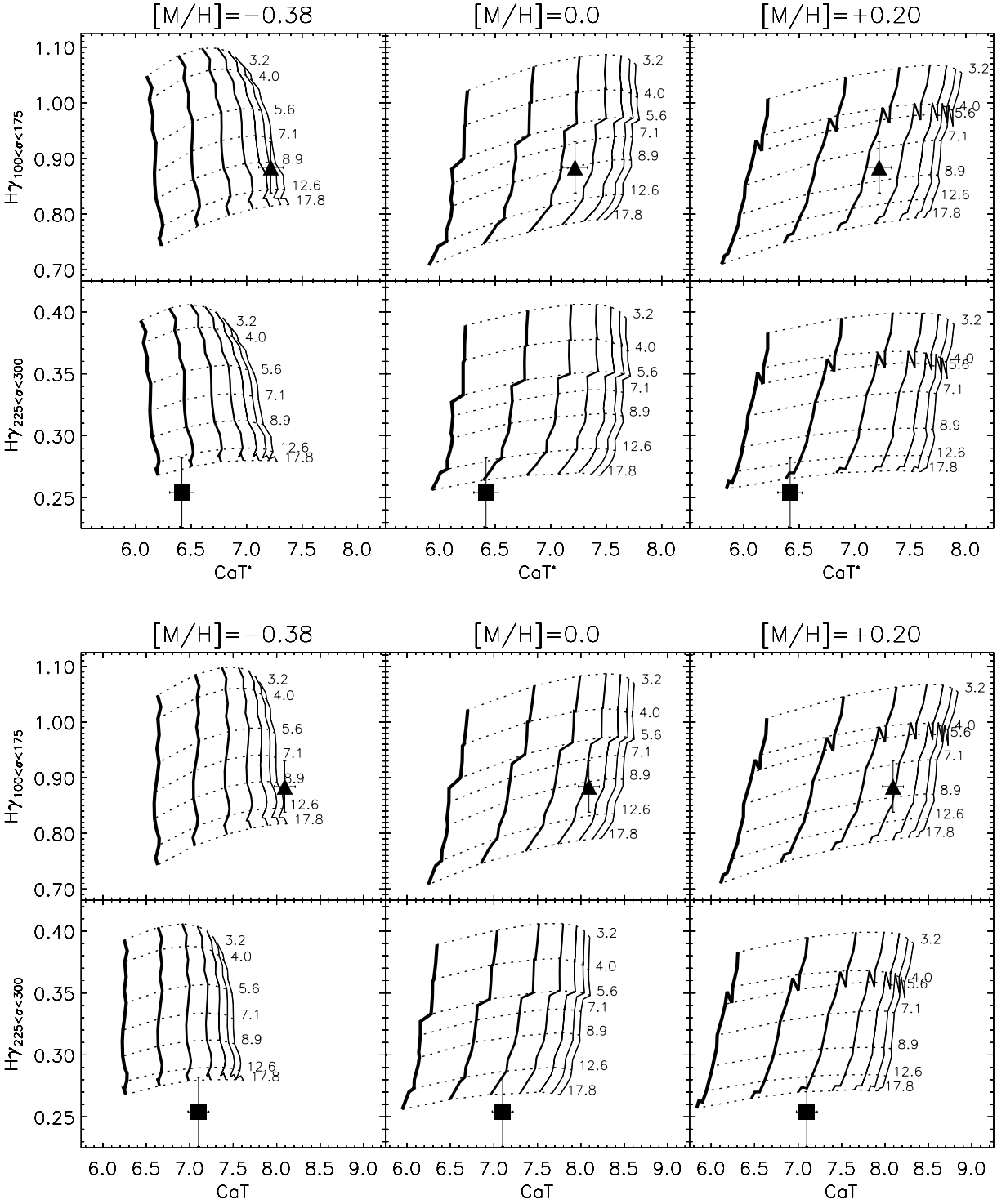

Figure 15. Plots of CaT* and CaT indices versus the Hγ_σ age indicators of VA99. Filled symbols represent the index measurements for the central apertures (4 arcsec) of two galaxies in common between the samples of C03 (for the Ca II triplet indices) and V01A (for the Hγ indices). The triangle represents NGC 4478, whilst the square represents NGC 4365. Overplotted are the models by V99 for the Hγ indices and those from this paper for the Ca II triplet feature. All index measurements were performed after smoothing the model SEDs to the appropriate galaxy velocity dispersion and instrumental resolution. We increase the metallicity of the model grids from left- to right-hand panels as quoted in the upper plots. We use a unimodal IMF, varying in each panel its slope from $\mu =$ 0.3 (thinnest vertical line) to $\mu = 3.3$ (thickest) by steps of $\Delta\mu = 0.5$. The third vertical line starting from the thinnest (i.e. right) corresponds to the Salpeter (1955) value (i.e. $\mu = 1.3$). Finally, thin dotted horizontal lines represent models of constant ages, which are quoted in gigayears.

We vary this slope, indicated by the strength of the line, from $\mu = 0.3$ (thinnest) to $\mu = 3.3$ (thickest) in steps of $\Delta\mu = 0.5$. The third vertical line starting from the thinnest (i.e. right) corresponds to the Salpeter (1955) value (i.e. $\mu = 1.3$). Models of constant age are shown by thin dotted horizontal lines.

All the model grids of Fig. 15 look rather orthogonal, which indicates that for a given metallicity we are able to separate the effects of age from those of the IMF slope. According to these plots, smaller $H\gamma_\sigma$ values mean larger ages and smaller CaT* or CaT indices mean steeper IMF slopes (i.e. dwarf-dominated). We see that the inferred ages do not depend on the metallicity of the model grid in use owing to the insensitivity of $H\gamma_\sigma$ to this parameter. Moreover, the fact that the Ca II triplet indices are insensitive to the metallicity for the range of metallicities covered in these plots ($-0.38 \leqslant$ [M/H] $\leqslant +0.2$) makes it possible to provide almost unique IMF slope solutions. All the diagrams indicate a mean luminosity-weighted age of $\sim$9 Gyr for NGC 4478 and $\simeq$15 Gyr for the giant elliptical galaxy NGC 4365. It is worth noting that the signal-to-noise ratio of the NGC 4365 spectrum was not high enough for an accurate measurement of the $H\gamma_\sigma$ index. However, the obtained age is not different from that derived on the basis of the $H\beta$ index (see V01A), and the age estimate given in Davies et al. (2001) from integral field spectroscopy. From the $H\gamma_\sigma$ versus CaT* diagrams we find $\mu \sim 2.3$ for NGC 4478 and $\mu \sim 2.8$ for NGC 4365, which indicate rather steep IMFs in comparison with the Salpeter value. However, it is worth recalling that variations in the theoretical prescriptions adopted for building up the stellar tracks and isochrones might drive to important changes in the predicted IMF slope. In fact, if we replace the model grids of Fig. 15 with another set synthesized on the basis of the old Padova isochrones (i.e. B94), which yield smaller CaT* strengths (i.e. ~ -0.5 Å) as a result of a slightly cooler RGB phase (see Appendix C2 for details on the differences in the adopted theoretical prescriptions), we would have obtained $\mu \sim 1.3$ for NGC 4478 and $\mu \sim 1.8$ for NGC 4365 (the $H\gamma_\sigma$ age indicator does not vary significantly as a result of this replacement, see V01B). Therefore, these results must be taken into account on a relative basis, whereas the discussion concerning galaxy trends is more secure (C03).

In Fig. 16 we plot the CaT* index versus different metallicity indicators in the blue spectral range, i.e. [MgFe] (González 1993), Mg*b* (W94), Fe3 (K00) and Ca 4227 (W94). In order to be able to show on a single plot the two galaxies we have smoothed the spectrum of NGC 4478 to match the resolution of NGC 4365. Each panel shows an approximately orthogonal model grid, with the position of the grid varying from the left- to the right-hand panels as a function of increasing metallicity. We, therefore, are unable to obtain a robust age determination on the basis of this figure. However, if we adopt for these galaxies the ages inferred from Fig. 15 we are in position to obtain the metallicity. The [MgFe]–CaT* diagrams suggest $[M/H]_{[MgFe]} \sim +0.1$ for NGC 4478 and solar metallicity for NGC 4365. From the Mg*b*–CaT* diagrams we obtain $[M/H]_{Mgb} \sim +0.2$ for the two galaxies. The Fe3–CaT* plots suggest $[M/H]_{Fe3} \sim 0.0$ for NGC 4478 and $[M/H]_{Fe3} \sim -0.1$ for NGC 4365. Finally, from the Ca 4227–CaT* diagrams we obtain $[M/H]_{Ca\,4227} \sim -0.2$ for NGC 4478 and $[M/H]_{Ca\,4227} \sim -0.4$ for NGC 4365. Interestingly, despite the fact that NGC 4365 is a larger galaxy, its metallicity seems to be slightly lower than that obtained for NGC 4478.

Fig. 16 shows us that the obtained metallicities are strongly influenced by non-solar abundance ratios in agreement with previous determinations (e.g. see, for recent references, K00; T00; V01A and PS02). Particularly interesting is the fact that the lowest metallicities are inferred when using the Ca 4227–CaT* diagrams. Despite the fact that Ca, similarly to Mg, is an α-element, Ca 4227 does not track Mg*b* (see V97; Peletier et al. 1999; T00; V01A; PS02). Although this result is in disagreement with our present knowledge of the nucleosynthesis theory (Woosley & Weaver 1995), if these galaxies were deficient in Ca, causing the Ca 4227 line to be smaller than predicted by scaled-solar models, we should consider the possibility that the Ca II triplet feature might be reflecting this deficiency as well. This suggests, as an alternative scenario, that the IMF is Salpeter-like and the low Ca II triplet values are a result of Ca deficiencies rather than from the steepening of the IMF.

A possible approach that can be followed for interpreting these results is to build-up SSP predictions based on non-solar abundance ratios. Such isochrones were predicted by, for example, SW98, S00, VandenBerg et al. (2000), Kim et al. (2002), for several α-enhancement ratios. These calculations were motivated by the finding that elliptical galaxies show an enhancement of Mg over Fe when compared with scaled-solar stellar population model predictions (e.g. Peletier 1989; Worthey et al. 1992; K00; V01A). However, to predict stellar population models of different α-enhancement ratios we require stellar tracks built up on the basis of appropriate opacity tables and energy generations, and the corresponding α-enhanced stellar spectral libraries. It is not yet clear what ratios should be adopted for the different α-elements. In fact, such α-enhancement stellar models have been calculated by various authors assuming a constant enhancement for each α-element (e.g. VandenBerg et al. 2000; Kim et al. 2002), or a somewhat more empirically based element mixture (e.g. SW98; S00). Furthermore, Ca 4227 does not track Mg (e.g. V97). However, such theoretical stellar spectral libraries are not yet available and all the empirical libraries such as that used here mostly follow the Galactic disc element ratios, particularly for the metallicity regime characteristic of the galaxies shown in Fig. 16 (i.e. around solar). Amongst the most important effects of adopting such isochrones is the fact that, for a given total metallicity, the α-enhanced mixtures lead to lower opacities, which translates into an increase of the temperature of the stars in both the main sequence and the RGB phases. However, for a given [Fe/H] metallicity, we obtain the opposite trend since the total metallicity of the α-enhanced models is larger. Another important result from these studies is that, for metal-rich stellar populations, α-enhanced isochrones cannot be mimicked with a scaled-solar isochrone of different metallicity.

Although it would be interesting to have models with varying [Ca/Fe] ratios as well, stellar libraries and isochrones calculated with such abundance ratios are not yet available. Moreover, it is not clear how we expect [Ca/Fe] to behave. It is worth noting that we did not obtain any significant correlation of the [Ca/Fe] abundance ratios with the residuals of the predictions of the fitting functions and the observed values for the Ca II triplet in our stellar library (Paper III). Despite the fact that we are not in a position to build up such fully self-consistent non-solar element ratios SSP models, we have tested in Appendix C2 the effects of adopting the α-enhanced isochrones of S00. These isochrones are calculated on the basis of the same input physics as that used in G00 for old stellar populations. For total metallicity [M/H] $\geqslant 0$ we obtain larger CaT* strengths (ΔCaT* ~ 0.5 Å). If we plot these model predictions in Fig. 15 we obtain even steeper IMF slopes. Alternatively, if a Salpeter-like IMF is used, the α-enhanced isochrones lead to a larger calcium underabundance problem.

It is, however, interesting to see how the model spectra of the adopted IMF slopes, ages and metallicities match the full spectral region around the Ca II triplet feature for these galaxies. In Fig. 17 we show the spectra of NGC 4478 (top panel) and NGC 4365 (bottom

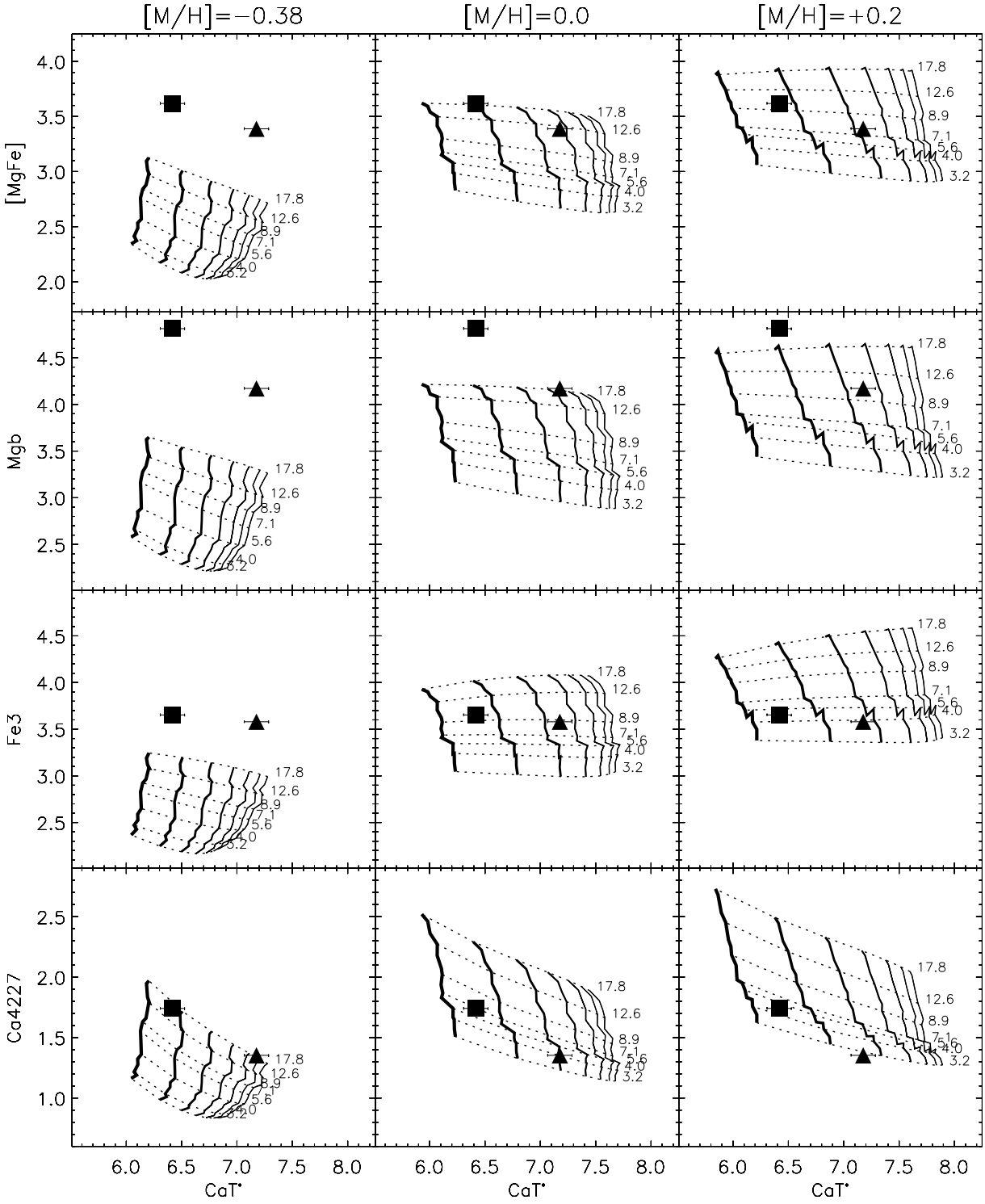

Figure 16. Plots of CaT* versus different metallicity indicators in the blue spectral region. Lines and symbols have the same meaning as in Fig. 15. In these plots all index measurements were obtained at resolution $\sigma_{\rm total} = 260$ km s^{-1}. The blue indices are taken from V01A.

panel). For NGC 4478 we overplot several models of age 9 Gyr as suggested by Fig. 15. In order to illustrate the effect of the IMF slope we have chosen two model spectra corresponding to $\mu = 1.3$ (as a reference) and $\mu = 2.3$ (the most suitable fit, according to Figs 15 and 16). The selected metallicity is around solar according to the [MgFe] and Fe3 indices. All the spectra were normalized according to the flux measured in the spectral region λλ8619–8642. It is apparent that the reference model with $\mu = 1.3$ provides slightly deeper Ca II triplet lines than observed in the galaxy spectrum. We also see that the model with $\mu = 2.3$ provides a better fit to the whole spectral region, including the slope of the continuum around the Ca II triplet feature. Finally, we overplot another model spectrum

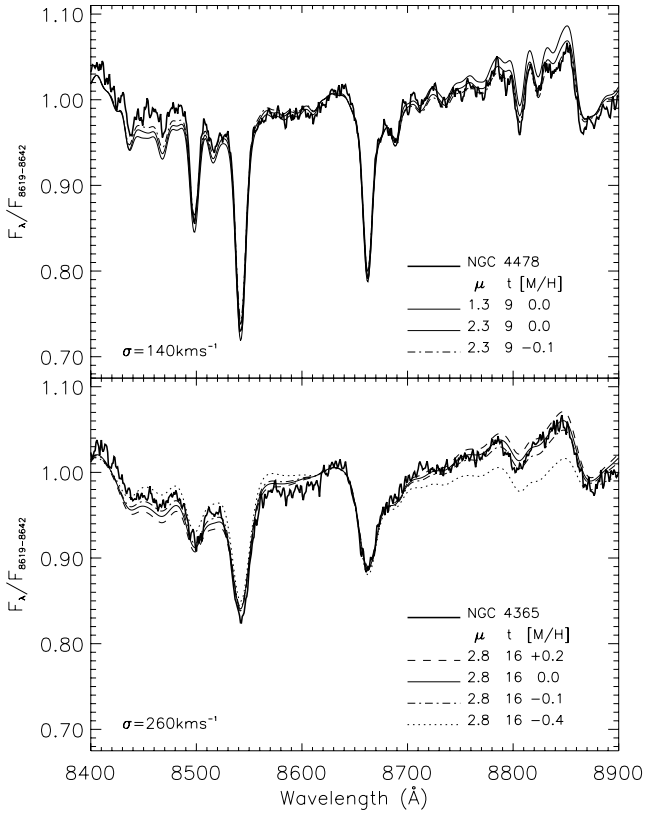

Figure 17. Spectra of NGC 4478 (upper panel) and NGC 4365 (lower panel). Overplotted are several model spectra selected on the basis of Figs 15 and 16, (see the text for details). All the spectra were normalized according to the flux measured in the spectral region λλ8619–8642.

of $\mu = 2.3$ and [M/H] $= -0.1$, which seems to provide a somewhat better fit to the overall galaxy spectrum.

In the lower panel of Fig. 17 we plot the spectrum of NGC 4365 and overplot several model spectra of similar age (15.85 Gyr) and IMF slope ($\mu = 2.8$). The four overplotted models were selected to have the metallicities inferred on the basis of the four metallicity indicators studied in Fig. 16. Overall, we see that the best fits are achieved for the metallicities in the range $-0.2 \leqslant$ [M/H] $\leqslant +0.1$, in good agreement with the predictions obtained on the basis of the [MgFe] (i.e. ∼0.0) and Fe3 (i.e. ∼−0.1) indices. On the other hand, the models of metallicities obtained from the Mg*b* (i.e. ∼+0.2) and Ca 4227 (i.e. ∼ −0.4) provides slightly steep and rather flat continua around the Ca II triplet feature, respectively. This result suggests that the metallicity inferred on the basis of the Fe3 and [MgFe] indices provide reasonably good fits to the overall spectrum in this spectral range.

9 CONCLUSIONS

We have presented a new evolutionary stellar population synthesis model in the near-IR spectral region covering the range λλ8350–8950 at a spectral resolution of 1.5 Å (FWHM). The ultimate aim of the models is to derive reliable predictions of the Ca II triplet strength for stellar populations over a wide range of ages, metallicities and IMF shapes. Apart from spectral energy distributions, the model predicts measurements in a set of new line indices, namely CaT*, CaT and PaT, which we have defined in Paper I to overcome some of the limitations of previous Ca II triplet index definitions in this spectral range. In particular, the CaT* index is particularly suited to removing the contamination from Paschen lines in the integrated spectra of galaxies.

The stellar population model presented here is a revised version of the model of V96 and V99. Several aspects of the model have been updated in order to produce a state-of-the-art output. The isochrones of B94 have been replaced by the newest Padova isochrones (G00), based on solar abundance ratios. The theoretical parameters of the predicted stars have been transformed to fluxes and colours on the basis of almost fully empirical relations based on extensive photometric stellar libraries. Apart from the IMF shapes used in V96 we use the two multipart power-law IMFs recently proposed by K01. The main ingredient for the predictions presented here, is the new extensive empirical stellar spectral library presented in Papers I and II, from which a subsample composed of more than 600 stars has been carefully selected. The sample shows an unprecedented coverage of the stellar atmospheric parameters ($T_{\rm eff}$, log g and [M/H]) for stellar population synthesis modelling.

Two main products of interest for stellar population analysis are presented: (i) a spectral library for SSPs with metallicities $-1.7 <$ [Fe/H] $< +0.2$, a large range of ages (0.1–18 Gyr) and IMF types and (ii) line-strengths calculated on the basis of the empirical fitting functions presented in Paper III for the CaT*, CaT and PaT indices, and for which conversion formulae to previous definitions can be found in Paper I. Tables and model spectra are available electronically at the web pages given in Section 3, together with the Ca II triplet stellar library.

The newly synthesized model spectra can be used to analyse observed galaxy spectrum in a safe and flexible way, allowing us to adapt the theoretical predictions to the nature of the data instead of proceeding in the opposite direction. The synthetic SSP library, with flux-calibrated spectral response, can be smoothed to the same resolution of the observations or to the measured internal galaxy velocity dispersion, making it possible to fully use all the information in the data. This opens the way (as do the models of V99 for the blue spectral region) for new applications. For example, if part of the spectrum is corrupted or affected by strong sky-lines, one can easily define new absorption lines on both models and data. Also, these models can be used as templates for determining stellar kinematics in galaxies (see Falcón-Barroso et al. 2003). Moreover, the models offer us a great opportunity to accurately study galaxies at larger redshifts.

We have analysed in detail the behaviour of the Ca II triplet feature in old-aged SSPs, finding the following results: (i) the strength of the CaT* index does not vary much for ages larger than ∼3 Gyr, for all metallicities; (ii) this index shows a strong dependence as a function of metallicity for values below [M/H] ∼−0.5; and (iii) for higher metallicities, this index does not show any significant dependence either on age or on the metallicity, being more sensitive to changes in the slope of power-like IMF shapes. These models open up the analysis of a suitable dwarf–giant discriminator in the analysis of stellar populations in galaxies. It is worth noting that the saturation of the Ca II triplet feature for metallicities above −0.5 has not been predicted by previous models. This prediction might be supported by the most metal-rich Galactic globular clusters and galaxy data analysed here. Furthermore, it might also be supported by the measurements of the CaT* and CaT indices in large samples of elliptical galaxies (Saglia et al. 2002; C03) and bulges (Falcón-Barroso et al. 2002).

For stellar populations in the age interval 0.1–1 Gyr we find that the Paschen lines, as defined by the PaT index, become more prominent and the CaT* index decreases significantly. However, the two

effects are compensated in the CaT in such a way that this index is virtually constant along this age range. Another interesting result is that the overall shape of the continuum around the Ca II triplet feature for large metallicities resembles more that of M-type stars rather than that of K-giants (as is the case for the blue spectral range).

By comparing globular cluster data (Section 8.1) we show that the derived metallicities are in excellent agreement with those from the literature, probing the validity of using the integrated Ca II triplet feature for determining metallicities for these stellar systems. It is worth noting that this is possible since the models predict that the Ca II triplet indices are virtually constant for stellar populations of ages larger than $\sim$3 Gyr and strongly dependent on metallicity for [M/H] < -0.5.

In Section 8.2 we have applied the models to two early-type galaxies of different luminosities, NGC 4478 and 4365 (from C03), for which a detailed stellar population analysis based on the optical spectral range was published in V01A. We propose several index–index diagrams, i.e. CaT* versus several age indicators, and CaT* versus several metallicity indicators, which provide virtually orthogonal model grids from which to disentangle, unambiguously, the relevant parameters of their stellar populations. The Ca abundance as inferred from the Ca II triplet does not follow Mg, as nucleosynthesis calculations predict, in agreement with measurements of the Ca 4227 line in the blue (V97). We should, however, note that Ca II triplet measurements cannot be fitted unless a very dwarf-dominated IMF is imposed, or unless the Ca abundance, as measured from the Ca II triplet, is even lower than the Fe abundance. However, it is worth recalling that variations in the theoretical prescriptions adopted for building up the stellar tracks and isochrones might lead to significantly lower IMF slope estimates and, therefore, these results must be taken into account on a relative basis, making the discussion concerning galaxy trends more secure (see, e.g., Saglia et al. 2002; C03). Moreover, if we adopted α-enhanced isochrones we would obtain steeper IMF slopes compared with scaled-solar. Alternatively, if a Salpeter-like IMF is used, the α-enhanced isochrones lead to a larger calcium underabundance problem. It is also important to note that the overall shape of the spectrum around the Ca II triplet feature and in particular the characteristic slope of the continuum is significantly better represented by choosing SSPs of metallicities as inferred from Fe or [MgFe] indices, rather than those based on the Mg*b* or Ca 4227 lines. More details can be found in C03, where a large sample of ellipticals are discussed in detail, revealing very interesting trends.

ACKNOWLEDGMENTS

We are indebted to the Padova group for making available their isochrone calculations. We are grateful to R. Schiavon for providing us with a set of synthetic spectra of SSPs and stars, as well as for very interesting discussions. This work was supported in part by a British Council grant within the British/Spanish Joint Research Programme (Acciones Integradas) and by the Spanish Programa Nacional de Astronomía y Astrofísica under grant no AYA2000-974. This work is based on observations at the JKT, INT and WHT on the island of La Palma operated by the Isaac Newton Group at the Observatorio del Roque de los Muchachos of the Instituto de Astrofísica de Canarias.

REFERENCES

Alexander D.R., Ferguson J.W., 1994, ApJ, 437, 879
Alonso A., Arribas S., Martínez-Roger C., 1995, A&A, 297, 197
Alonso A., Arribas S., Martínez-Roger C., 1996, A&A, 117, 227
Alonso A., Arribas S., Martínez-Roger C., 1999, A&AS, 140, 261
Alloin D., Bica E., 1989, A&A, 217, 57
Arimoto N., Yoshii Y., 1986, A&A, 164, 260
Armandroff T.E., Zinn R., 1988, AJ, 96, 92 (AZ88)
Bender R., Burstein D., Faber S.M., 1993, ApJ, 411, 153
Bertelli G., Bressan A., Chiosi C., Fagotto F., Nasi E., 1994, A&AS, 106, 275 (B94)
Bessell M.S., 1979, PASP, 91, 589
Bessell M.S., Brett J.M., Wood P.R., Scholz M., 1989, A&AS, 77, 1
Bessell M.S., Brett J.M., Scholz M., Wood P.R., 1991, A&AS, 89, 335
Bica E., Alloin D., 1987, A&A, 186, 49
Blakeslee J.P., Vazdekis A., Ajhar E.A., 2001, MNRAS, 320, 193
Bower R.G., Lucey J.R., Ellis R.S., 1992, MNRAS, 254, 601
Bressan A., Chiosi C., Fagotto F., 1994, ApJS, 94, 63
Bruzual A.G., 1983, ApJ, 273, 105
Bruzual A.G., Charlot S., 1993, ApJ, 405, 538
Buzzoni A., 1993, A&A, 275, 433
Carretta E., Gratton R.G., 1997, A&AS, 121, 95
Carter D., Visvanathan N., Pickles A.J., 1986, ApJ, 311, 637
Cenarro A.J., 2002, PhD thesis, Universidad Complutense de Madrid, Spain
Cenarro A.J., Cardiel N., Gorgas J., Peletier R.F., Vazdekis A., Prada F., 2001a, MNRAS, 326, 959 (Paper I)
Cenarro A.J., Gorgas J., Cardiel N., Pedraz S., Peletier R.F., Vazdekis A., 2001b, MNRAS, 326, 981 (Paper II)
Cenarro A.J., Gorgas J., Cardiel N., Vazdekis A., Peletier R.F., 2002, MNRAS, 329, 863 (Paper III)
Cenarro A.J., Gorgas J., Vazdekis A., Cardiel N., Peletier R.F., 2003, MNRAS, 339, L12 (C03)
Charlot S., Worthey G., Bressan A., 1996, ApJ, 457, 625
Chmielewski Y., 2000, A&A, 353, 666
Code A.D., Bless R.C., Davis J., Brown R.H., 1976, ApJ, 203, 417
Cohen J.G., 1978, ApJ, 221, 788
Cohen J.G., 1979, ApJ, 228, 405
Colless M., Burstein D., Davies R.L., McMahan R., Saglia R., Wegner G., 1999, MNRAS, 303, 813
Davies R.L. et al., 2001, ApJ, 548, L33
Díaz A.I., Terlevich E., Terlevich R., 1989, MNRAS, 239, 325
Ellis R.S., Smail I., Dressler A., Couch W.J., Oemler A., Jr, Butcher H., Sharples R.M., 1997, ApJ, 483, 582
Erdelyi-Mendes M., Barbuy B., 1991, A&A, 241, 176
Faber S.M., French H.B., 1980, ApJ, 235, 405
Faber S.M., Trager S.C., González J.J., Worthey G., 1995, in van der Kruit P.C., Gilmore G., eds, Proc. IAU Symp. 164, Stellar Populations. Kluwer, Dordrecht, p. 249
Falcón-Barroso J., Peletier R.F., Vazdekis A., Balcells M., 2002, ApJ, submitted
Falcón-Barroso J., Balcells M., Peletier R.F., Vazdekis A., 2003, A&A, in press
Fluks M.A., Plez B., Thé P.S., de Winter D., Westerlund B.E., Steenman H.C., 1994, A&AS, 105, 311
Forbes D.A., Boisson C., Ward M.J., 1992, MNRAS, 259, 293
García-Vargas M.L., Díaz A.I., Terlevich E., Terlevich R., 1993, Ap&SS, 205, 85
García-Vargas M.L., Mollá M., Bressan A., 1998, A&AS, 130, 513
Girardi L., Bressan A., Bertelli G., Chiosi C., 2000, A&AS, 141, 371 (G00)
González J.J., 1993, PhD thesis, Univ. California, Santa Cruz
González Delgado R.M., Pérez E., 1996a, MNRAS, 278, 737
González Delgado R.M., Pérez E., 1996b, MNRAS, 280, 53
Gorgas J., Faber S.M., Burstein D., González J.J., Courteau S., Prosser C., 1993, ApJS, 86, 153
Gorgas J., Cardiel N., Pedraz S., González J.J., 1999, A&AS, 139, 29
Heckman T.M., González Delgado R., Leitherer C., Meurer G.R., Krolik J., Wilson A.S., Koratkar A., Kinney A., 1997, ApJ, 482, 114
Houdashelt M.L., 1995, PhD thesis, Ohio State Univ.
Idiart T.P., Thévenin F., de Freitas Pacheco J.A., 1997, AJ, 113, 1066 (ITD)
Johnson H.L., 1966, ARA&A, 4, 193
Jones J.E., Alloin D.M., Jones B.J.T., 1984, ApJ, 283, 457

Jones L.A., 1999, PhD thesis, Univ. North Carolina, Chapel Hill
Jones L.A., Worthey G., 1995, ApJ, 446, L31
Jørgensen I., 1999, MNRAS, 306, 607
Jørgensen U.G., Carlsson M., Johnson H.R., 1992, A&A, 254, 258
Kim Y., Demarque P., Yi S., Alexander D.R., 2002, ApJS, 143, 499
Kodama T., Arimoto N., 1997, A&A, 320, 41
Kholopov P.N. et al., 1998, The Combined General Catalogue of Variable Stars, 4th edn, Moscow Sternberg Astron. Institute, http://vizier.u-stasbg.fr/II/214A
Kroupa P., 2001, MNRAS, 322, 231 (K01)
Kroupa P., Tout C.A., Gilmore G., 1993, MNRAS, 262, 545
Kuntschner H., 2000, MNRAS, 315, 184 (K00)
Kurth O.M., Fritze-V. Alvensleben U., Fricke K.J., 1999, A&AS, 138, 19
Kurucz R.L., 1992, in Barbuy B. Renzini A., eds, The Stellar Populations of Galaxies. Dordrecht, Kluwer, p. 225
Lejeune T., Cuisinier F., Buser R., 1997, A&AS, 125, 229
Lejeune T., Cuisinier F., Buser R., 1998, A&AS, 130, 65
Mallik S.V., 1994, A&AS, 103, 279
Mallik S.V., 1997, A&AS, 124, 359
Maraston C., Thomas D., 2000, ApJ, 541, 126
Mayya Y.D., 1997, ApJ, 482, L149
Mollá M., García-Vargas M.L., 2000, A&A, 359, 18 (MGV)
O'Connell R.W., 1976, ApJ, 206, 370
Peletier R.F., 1989, PhD thesis, Univ. Groningen
Peletier R.F., 1999, in Beckman J.E Mahoney T.J., eds, ASP Conf. Ser. Vol. 187, The Evolution of Galaxies on Cosmological Timescales. Astron. Soc. Pac., San Francisco, p. 231
Peletier R.F., Vazdekis A., Arribas S., del Burgo C., García-Lorenzo B., Gutiérrez C., Mediavilla E., Prada F., 1999, MNRAS, 310, 863
Pérez E., Márquez I., Marrero I., Durret F., González Delgado R.M., Masegosa J., Maza J., Moles M., 2000, A&A, 353, 893
Pickles A.J., 1998, PASP, 110, 863
Poggianti B.M. et al., 2001, ApJ, 562, 689
Pols O.R., Tout C.A., Eggleton P.P., Han Z., 1995, MNRAS, 274, 964
Ponder J.M. et al., 1998, AJ, 116, 2297
Proctor R.N., Sansom A.E., 2002, MNRAS, 333, 517 (PS02)
Ridgway S.T., Joyce R.R., White N.M., Wing R.F., 1980, ApJ, 235, 126
Rutledge G.A., Hesser J.E., Stetson P.B., 1997, PASP, 109, 907
Saglia R.P., Maraston C., Thomas D., Bender R., Colless M., 2002, ApJ, 579, L13
Salaris M., Weiss A., 1998, A&A, 335, 943 (SW98)
Salaris M., Groenewegen M., Weiss A., 2000, A&A, 355, 299
Salasnich B., Girardi L., Weiss A., Chiosi C., 2000, A&A, 361, 1023 (S00)
Salpeter E.E., 1955, ApJ, 121, 161
Scalo J.M., 1986, Fundam. Cosmic Phys, 11, 1
Schiavon R.P., Barbuy B., 1999, ApJ, 510, 934
Schiavon R.P., Barbuy B., Bruzual G., 2000, ApJ, 532, 453 (SBB)
Smith G., Drake J.J., 1987, A&A, 181, 103
Smith G., Drake J.J., 1990, A&A, 231, 125
Stanford S.A., Elston R., Eisenhardt P.R., Spinrad H., Stern D., Dey A., 1997, AJ, 114, 2232
Tantalo R., Chiosi C., Bressan A., 1998, A&A, 333, 419
Terlevich E., Díaz A.I., Terlevich R., 1990a, MNRAS, 242, 271
Terlevich E., Terlevich R., Díaz A.I., Pastoriza M.G., Dottori H., 1990b, MNRAS, 242, 48
Terlevich A.I., Kuntschner H., Bower R.G., Caldwell N., Sharples R.M., 1999, MNRAS, 310, 445
Tinsley B.M., 1980, Fundam. Cosmic Phys., 5, 287
Trager S.C., Worthey G., Faber S.M., Burstein D., González J.J., 1998, ApJS, 116, 1
Trager S.C., Faber S.M., Worthey G., González J.J., 2000a, AJ, 119, 1645
Trager S.C., Faber S.M., Worthey G., González J.J., 2000b, AJ, 120, 165 (T00)
VandenBerg D.A., Swenson F.J., Rogers F.J., Iglesias C.A., Alexander D.R., 2000, ApJ, 532, 430
Vazdekis A., 1999, ApJ, 513, 224 (V99)
Vazdekis A., Arimoto N., 1999, ApJ, 525, 144 (VA99)
Vazdekis A., Casuso E., Peletier R.F., Beckman J.E., 1996, ApJS, 106, 307 (V96)
Vazdekis A., Peletier R.F., Beckman J.E., Casuso E., 1997, ApJS, 111, 203 (V97)
Vazdekis A., Kuntschner H., Davies R.L., Arimoto N., Nakamura O., Peletier R.F., 2001a, ApJ, 551, L127 (V01A)
Vazdekis A., Salaris M., Arimoto N., Rose J.A., 2001b, ApJ, 549, 274 (V01B)
Woosley S.E., Weaver T.A., 1995, ApJS, 101, 181
Worthey G., 1994, ApJS, 95, 107
Worthey G., 1998, PASP, 110, 888
Worthey G., Ottaviani D.L., 1997, ApJS, 111, 377 (WO97)
Worthey G., Faber S.M., González J.J., 1992, ApJ, 398, 69
Worthey G., Faber S.M., González J.J., Burstein D., 1994, ApJS, 94, 687 (W94)
Zhou X., 1991, A&A, 248, 367
Zinn R., West M.J., 1984, ApJS, 55, 45

APPENDIX A: THE IMF TYPES

In this appendix we summarize all the IMFs used in this paper, which include the two IMF shapes given by V96, i.e. unimodal and bimodal, and the new IMFs proposed by K01, i.e. universal and revised. These four IMF shapes are plotted in Fig. 1.

The unimodal IMF has a power-law form characterized by its slope μ as a free parameter

$$\Phi(m) = \beta m^{-(\mu+1)}. \tag{A1}$$

Therefore, the Salpeter (1955) solar neighbourhood IMF is obtained when $\mu = 1.3$.

The bimodal IMF is similar to the unimodal case for stars with masses above 0.6 $M_\odot$, but decreasing the weight of the stars with lower masses by means of a transition to a shallower slope, which becomes flat in the $\log\{\Phi[\log(m)]\}$–$\log(m)$ diagram for masses lower than 0.2 $M_\odot$. The main motivation for this IMF is to achieve a reasonable good fit to the observational data of Scalo (1986) and Kroupa, Tout & Gilmore (1993) on the basis of a single free parameter, i.e. μ, rather than using several segments as it is the case for the IMFs of K01. The main advantage of the bimodal IMF is that it allows us to vary the parameter μ in the same way as for the unimodal case. The form of this IMF[1] is given by

$$\Phi(m) = \beta \begin{cases} \dfrac{m_1^{-\mu}}{m}, & m \leqslant m_0 \\ p(m), & m_0 < m \leqslant m_2 \\ m^{-(\mu+1)}, & m > m_2, \end{cases} \tag{A2}$$

where m_0, m_1 and m_2 are 0.2, 0.4 and 0.6 $M_\odot$, respectively. $p(m)$ is a spline for which we calculate the corresponding coefficients solving for the following system obtained by the boundary conditions:

$$\begin{aligned} p(m_0) &= m_1^{-\mu}, \\ p'(m_0) &= 0, \\ p(m_2) &= m_2^{-\mu}, \\ p'(m_2) &= -\mu m_2^{-(\mu+1)}. \end{aligned} \tag{A3}$$

In this paper we have introduced the two IMF shapes recently proposed by K01. The universal IMF is a multipart power-law IMF, which has the following form:

[1] Note the erratum present in equation (4) (case $m \leqslant 0.2\ M_\odot$) of V96, which should be divided by m.

$$\Phi(m) = \beta \begin{cases} \left(\frac{m}{m_0}\right)^{-0.3}, & m \leqslant m_0 \\ \left(\frac{m}{m_0}\right)^{-1.3}, & m_0 < m \leqslant m_1 \\ \left(\frac{m_1}{m_0}\right)^{-1.3}\left(\frac{m}{m_1}\right)^{-2.3}, & m > m_1, \end{cases} \quad \text{(A4)}$$

where m_0 and m_1 are 0.08 and 0.5 $M_\odot$, respectively.

We have also implemented the revised multipart power-law IMF of K01, which tries to correct for the systematic effects owing to unresolved binaries on the single-star IMF. The main effect is that the slope of the IMF is steeper than the universal IMF by $\Delta\mu \sim 0.5$ for the mass range $0.08 < m < 1$ $M_\odot$. Its shape is summarized in the following equation:

$$\Phi(m) = \beta \begin{cases} \left(\frac{m}{m_0}\right)^{-0.3}, & m \leqslant m_0 \\ \left(\frac{m}{m_0}\right)^{-1.8}, & m_0 < m \leqslant m_1 \\ \left(\frac{m_1}{m_0}\right)^{-1.8}\left(\frac{m}{m_1}\right)^{-2.7}, & m_1 < m \leqslant m_2 \\ \left(\frac{m_1}{m_0}\right)^{-1.8}\left(\frac{m_2}{m_1}\right)^{-2.7}\left(\frac{m}{m_2}\right)^{-2.3}, & m > m_2, \end{cases} \quad \text{(A5)}$$

where m_0, m_1 and m_2 are 0.08, 0.5 and 1 $M_\odot$, respectively.

Finally, the constant β is calculated via the normalization

$$\beta \int_{m_l}^{m_u} \Phi(m)\,\mathrm{d}m = 1, \quad \text{(A6)}$$

where m_l and m_u are the lower and upper mass cut-offs. We adopt 0.01 and 120 $M_\odot$ for these stellar masses, respectively.

APPENDIX B: COMPUTATION OF A REPRESENTATIVE STELLAR SPECTRUM

We provide here a detailed description of how we interpolate spectra in the data base and compute the spectrum corresponding to a given set of requested parameters (θ_0, log g_0 and [M/H]$_0$). The most straightforward approach to follow is to let the code find all the stars enclosed within a given cube centred on these atmospheric parameters. However, since in many cases there is a lack of symmetry in the distribution of stars around a given point in the three-parameter space, we have divided the original box in eight cubes all with one corner at θ_0, log g_0, [M/H]$_0$. In this way we make sure that there are stars in all the directions with respect to the required point. The code finds all the stars N_j enclosed within a cube j (where $j = 1, \ldots, 8$) and combines their spectra according to

$$S_\lambda{}^j = \frac{\sum_{i=1}^{N_j} S_{\lambda i}{}^j W_i^j}{\sum_{i=1}^{N_j} W_i^j}, \quad \text{(B1)}$$

where W_i^j is the weight assigned to the star i within the cube j:

$$W_i^j = \left\{ \exp\left[-\left(\frac{\theta_i - \theta_0}{\sigma_{\theta_0}}\right)^2\right] \exp\left[-\left(\frac{\log g_i - \log g_0}{\sigma_{\log g_0}}\right)^2\right] \times \exp\left[-\left(\frac{[\mathrm{M/H}]_i - [\mathrm{M/H}]_0}{\sigma_{[\mathrm{M/H}]_0}}\right)^2\right] \right\} \mathrm{SN}_{n_i}, \quad \text{(B2)}$$

where SN_{n_i} is a measure of the quality of the empirical spectrum $S_{\lambda i}{}^j$ estimated by its signal-to-noise ratio normalized in the following way:

$$\mathrm{SN}_{n_i} = 1, \quad \mathrm{SN}_i \geqslant \mathrm{SN}_{99.7}$$

$$\mathrm{SN}_{n_i} = \frac{\mathrm{SN}_i^2}{\mathrm{SN}_{99.7}^2}, \quad \mathrm{SN}_i < \mathrm{SN}_{99.7}, \quad \text{(B3)}$$

where $\mathrm{SN}_{99.7}$ is the limiting SN value where the cumulative SN distribution fraction of our stellar sample reaches the upper 99.7 percentile [$\sum \mathrm{SN}_i(\mathrm{SN}_i < \mathrm{SN}_{99.7})/\sum \mathrm{SN}_i$]. We note, however, that a spectroscopic binary or a star with anomalous signature of high variability that is present in the stellar library (see Section 3.1.1) would be able to contribute significantly within a given cube if its SN_{n_i} is high. To prevent this possibility we have chosen to get down the SN_{n_i} of these stars to the value where the cumulative SN distribution fraction of our stellar sample reaches the lower 0.3 percentile.

The term within the curly brackets in equation (B2) represents the weight resulting from the position of the star i in the parameter space (θ, log g, [M/H]). We have assumed a Gaussian-like function, which assigns larger weights to the stars closer to the requested point (θ_0, log g_0, [M/H]$_0$). This term, as well as SN_{n_i}, varies from 0 to 1. The σ_{θ_0}, $\sigma_{\log g_0}$ and $\sigma_{[\mathrm{M/H}]_0}$ values (generically σ_{p0}) are estimated on the basis of the density of stars at the requested point in the parameter space ρ_0. We assumed an inversely proportional Gaussian-like function of the form

$$\sigma_{p_0} \propto \exp\left[\frac{1}{2}\left(\frac{\rho_0 - \rho_\mathrm{M}}{\sigma_{\rho_0}}\right)^2\right], \quad \text{(B4)}$$

where ρ_M is the maximum density. Assuming that the smallest σ_{p_m} is obtained at the point of maximum density (ρ_M) and that the largest σ_{p_M} is reached when $\rho \to 0$ we derive σ_{ρ_0} and then equation (B4) can be written as

$$\sigma_{\theta 0} = \sigma_{\theta \mathrm{m}} \exp\left[\left(\frac{\rho_0 - \rho_\mathrm{M}}{\rho_\mathrm{M}}\right)^2 \ln \frac{\sigma_{\theta \mathrm{M}}}{\sigma_{\theta \mathrm{m}}}\right]$$

$$\sigma_{\log g_0} = \sigma_{\log g_\mathrm{m}} \exp\left[\left(\frac{\rho_0 - \rho_\mathrm{M}}{\rho_\mathrm{M}}\right)^2 \ln \frac{\sigma_{\log g_\mathrm{M}}}{\sigma_{\log g_\mathrm{m}}}\right]$$

$$\sigma_{[\mathrm{M/H}]_0} = \sigma_{[\mathrm{M/H}]_\mathrm{m}} \exp\left[\left(\frac{\rho_0 - \rho_\mathrm{M}}{\rho_\mathrm{M}}\right)^2 \ln \frac{\sigma_{[\mathrm{M/H}]_\mathrm{M}}}{\sigma_{[\mathrm{M/H}]_\mathrm{m}}}\right]. \quad \text{(B5)}$$

We have assumed $\sigma_{\theta \mathrm{m}}$, $\sigma_{\log g_\mathrm{m}}$ and $\sigma_{[\mathrm{M/H}]\mathrm{m}}$ to be the minimum uncertainty in the determination of θ, log g and [M/H], respectively. We adopted $\sigma_{\theta \mathrm{m}} = 0.009$, $\sigma_{\log g_\mathrm{m}} = 0.18$ and $\sigma_{[\mathrm{M/H}]_\mathrm{m}} = 0.09$ according to the values given in Paper II. It is worth noting that the points where the uncertainties are the smallest coincide with the most populated regions of the parameter space, e.g. dwarfs of ~5800 K and giants of ~4800 K of solar metallicity. On the other hand, for $\sigma_{\theta \mathrm{M}}$, $\sigma_{\log g_\mathrm{M}}$ and $\sigma_{[\mathrm{M/H}]_\mathrm{M}}$ we assumed a range of 1/10 of the total covered by these parameters in our stellar library. We adopted $\sigma_{\theta \mathrm{M}} = 0.17$, $\sigma_{\log g_\mathrm{M}} = 0.51$ and $\sigma_{[\mathrm{M/H}]_\mathrm{M}} = 0.41$. For σ_θ we also assumed the condition that $60 \leqslant T_\mathrm{eff} \leqslant 3350$ K (corresponding to the adopted σ_θ limiting values when transforming to the T_eff scale).

At a given point ρ_0 is calculated by counting the number of stars present in a box of size $3 \times \sigma_{p_\mathrm{m}}$. If no stars are found, the box is simultaneously enlarged in its three dimensions, in steps of $1 \times \sigma_{p_\mathrm{m}}$, until at least one single star is reached. For stars with temperatures larger than 9000 K and lower than 4000 K we do not take into account the metallicity parameter, since its uncertainty is very large and since we adopted [Fe/H] = 0 for stars with unknown metallicity in these temperature ranges. In practice, we adopt ρ_M as the density value where the cumulative density fraction reaches the upper 99.7 percentile. For larger densities we adopt this value as well. An example of the resulting σ_θ, $\sigma_{\log g}$ and $\sigma_{[\mathrm{M/H}]}$ is shown in Fig. B1 for two

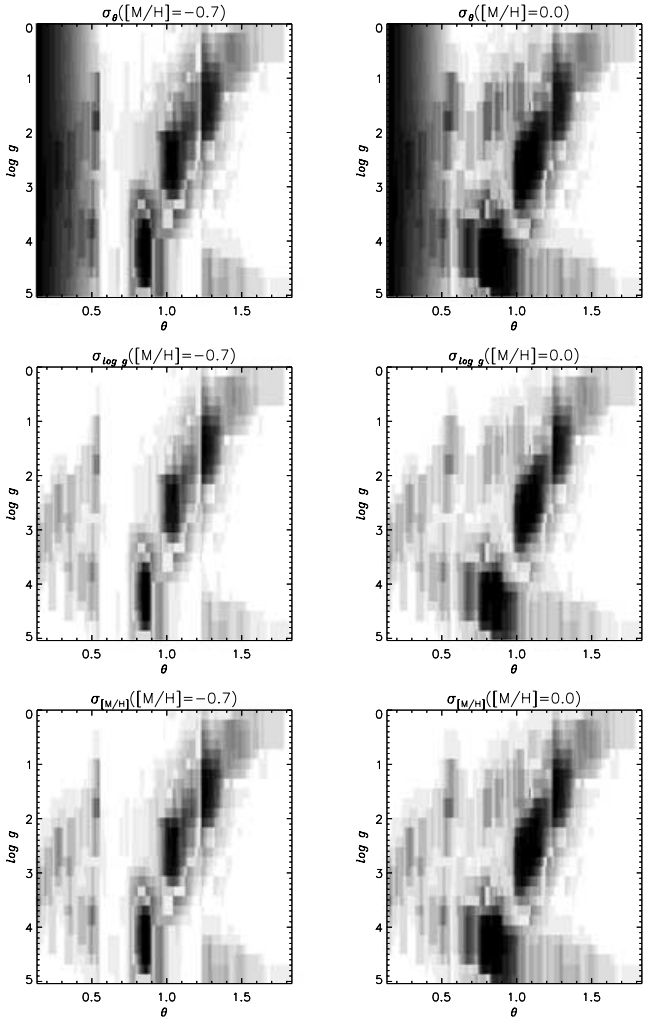

Figure B1. Grey levels representing the values of σ_θ, $\sigma_{\log g}$ and $\sigma_{[\mathrm{M/H}]}$ (from top to bottom plots), calculated for $[\mathrm{M/H}] = -0.7$ (left) and $[\mathrm{M/H}] = 0.0$ (right) in the θ–log g plane. Black means $\sigma_\theta = 0.009$, $\sigma_{\log g} = 0.18$ and $\sigma_{[\mathrm{M/H}]} = 0.09$, whereas white means $\sigma_\theta = 0.17$, $\sigma_{\log g} = 0.51$ and $\sigma_{[\mathrm{M/H}]} = 0.41$ in the corresponding plots.

values of the metallicity. Black means $\sigma_\theta = 0.009$, $\sigma_{\log g} = 0.18$ and $\sigma_{[\mathrm{M/H}]} = 0.09$, whereas white means $\sigma_\theta = 0.17$, $\sigma_{\log g} = 0.51$ and $\sigma_{[\mathrm{M/H}]} = 0.41$ in the corresponding plots. Overall, the grey levels for the plots corresponding to $[\mathrm{M/H}] = 0.0$ are significantly darker than those for $[\mathrm{M/H}] = -0.7$, owing to the fact that our library is more populated with solar metallicity stars. Note that the MS and RGB phases are clearly visible. An interesting feature is that for the σ_θ plots the grey levels become gradually darker towards hotter stars as a result of the fact that we assumed that the largest σ_θ value cannot be larger than 1/10 of total range in the T_{eff} scale. Note the jump in the grey levels when θ reaches values around 0.55 and 1.25 owing to the fact that for very hot or very cool stars we did not consider their metallicities. Obviously this jump is more pronounced for the plots corresponding to $[\mathrm{M/H}] = -0.7$.

Once the density is known and $\sigma_{\theta 0}$, $\sigma_{\log g_0}$ and $\sigma_{[\mathrm{M/H}]_0}$ have been estimated according to equation (B5), we find all the stars enclosed in each of the eight cubes of size $1.5\sigma_{p_0}$. For the most populated regions of the parameter space we find stars in all these eight cubes. However, if no stars are found in a given cube, we simultaneously enlarge its three sizes in steps of $0.5\times\sigma_{p_0}$. Since one of the corners of the cube is always located on the required parameter point itself, the box is enlarged to one side only. In the worst case, this iterative procedure ensures finding stars in, at least, three cubes. Finally, a similar criterion to that applied for calculating ρ_0 is taken into account for stars cooler than 4000 K and hotter than 9000 K, i.e. neglecting their metallicity.

Having obtained a representative spectrum for each cube, ${S_\lambda}^j$, we are now in a position to calculate $S_\lambda(m, t, [\mathrm{M/H}])$. The weight to be assigned to ${S_\lambda}^j$ is estimated as follows:

$$W^j = \exp\left[-\left(\frac{\theta^j - \theta_0}{\sigma_{\theta_0}}\right)^2\right] \exp\left[-\left(\frac{\log g^j - \log g_0}{\sigma_{\log g_0}}\right)^2\right]$$

$$\times \exp\left[-\left(\frac{[\mathrm{M/H}]^j - [\mathrm{M/H}]_0}{\sigma_{[\mathrm{M/H}]_0}}\right)^2\right], \qquad \text{(B6)}$$

where θ^j, $\log g^j$ and $[\mathrm{M/H}]^j$ are given by

$$\theta^j = \frac{\sum_{i=1}^{N_j} \theta_i^j W_i^j}{\sum_{i=1}^{N_j} W_i^j}$$

$$\log g^j = \frac{\sum_{i=1}^{N_j} \log g_i^j W_i^j}{\sum_{i=1}^{N_j} W_i^j}$$

$$[\mathrm{M/H}]^j = \frac{\sum_{i=1}^{N_j} [\mathrm{M/H}]_i^j W_i^j}{\sum_{i=1}^{N_j} W_i^j}. \qquad \text{(B7)}$$

We then solve for the following undetermined linear system of equations

$$\sum_{j=1}^{k} \alpha^j W^j \left(\theta^j - \theta_0\right) = 0$$

$$\sum_{j=1}^{k} \alpha^j W^j \left(\log g^j - \log g_0\right) = 0$$

$$\sum_{j=1}^{k} \alpha^j W^j \left([\mathrm{M/H}]^j - [\mathrm{M/H}]_0\right) = 0, \qquad \text{(B8)}$$

where k represents the number of available cubes that contain stars after the iterative procedure explained above ($3 \leqslant k \leqslant 8$), and α^j are coefficients to be applied for correcting the weights W^j to be assigned to the spectra ${S_\lambda}^j$ when combining them to obtain $S_\lambda(m, t, [\mathrm{M/H}])$. Only values in the range $0 \leqslant \alpha^j < 1$ are acceptable for these coefficients. Among the solutions we choose the one that minimizes the modification of the intrinsic weights W^j. This is performed by calculating the projection of the solution hyperplane on to the point ($\alpha^j = 1$, $j = 1, k$) of the k-dimensional space. When no non-negative α^j solutions can be found taking into account the k cubes, we start a procedure where we neglect the contribution of a given cube in equation (B8). This is performed following the criterion of removing first the cubes with lower intrinsic weights according to $\mathrm{SN}_n^j W^j$ where $\mathrm{SN}_n{}^j$[2] is given by

[2] Note that we do not adopt the true SN corresponding to ${S_\lambda}^j$ since the most populated cubes would be assigned considerably higher weights, an effect which tends to emphasize the asymmetries present in several regions of the parametric space.

$$\mathrm{SN}_n{}^j = \frac{\sum_{i=1}^{N_j} \mathrm{SN}_{n_i}{}^j W_i^j}{\sum_{i=1}^{N_j} W_i^j}. \quad \text{(B9)}$$

If no satisfactory solutions are found, we select the one which minimizes the difference between the required atmospheric parameters and those resulting from the solution star having taken into account α^j as in equation (B8). The final spectrum, $S_\lambda(m, t, [\mathrm{M/H}])$, is obtained as follows:

$$S_\lambda(m, t, [\mathrm{M/H}]) = \frac{\sum_{j=1}^{k} S_\lambda{}^j \alpha^j W^j}{\sum_{j=1}^{k} \alpha^j W^j}, \quad \text{(B10)}$$

where $S_\lambda{}^j$ are normalized to the selected wavelength reference interval $\Delta\lambda_{\mathrm{ref}}$ and scaled according to the derived $\alpha^j W^j$.

APPENDIX C: MODEL UNCERTAINTIES

In this Appendix we perform a number of tests to evaluate the major uncertainties affecting the obtained SSP model predictions presented in this paper. We first focus on the uncertainties derived from varying the model calculation details, particularly in the way that we compute a representative stellar spectrum. We then explore the effects of varying the adopted theoretical prescriptions for calculating the stellar evolutionary tracks and isochrones. To illustrate how significant a given effect is, we have chosen to measure the variation of the most important feature in this spectral range, i.e. the Ca II triplet, by means of the CaT* index.

C1 Uncertainties derived from the gridding of the stellar library

Here we study the effects of varying the way in which we compute a stellar spectrum according to the description given in Section 3.2 and, particularly, in Appendix B. We select for this purpose a representative set of SSP models of age 12.59 Gyr (old stellar populations are more sensitive to the lack of cool stars) and metallicities [M/H] = −0.68, −0.38, 0.0 and +0.2.

We first test to vary the lower temperature limit, below which the metallicities of the stars are not taken into account when calculating a representative spectrum corresponding to a given set of atmospheric parameters. Table C1 lists the obtained residuals for the CaT* index when increasing this temperature from the adopted value, i.e. 4000 K, to 4250 K, and when decreasing it to 3750 K. We note that above 4000 K the obtained differences change very softly. Varying this limit towards temperatures lower than 3750 K has virtually no effect when compared with the values obtained for this temperature limit, owing to the fact that most of the stars have either solar metallicity or have been assumed to be solar when no metallicity values were available in the literature. We conclude that this temperature limit is mostly affecting the integrated spectrum of SSPs of [M/H] = −0.68, but the largest variation in the CaT* index is ∼1 per cent of the CaT* index strength.

We also explored the effect of varying the density value ρ_{M} where the cumulative density fraction of stars reaches the upper percentile 99.7–100 and 90 (see Table C1). In practice for an upper percentile value of 100, this assumption means that there is a single point in the stellar parametric space where $\sigma_{\theta\mathrm{m}}$, $\sigma_{\log g_{\mathrm{m}}}$ and $\sigma_{[\mathrm{M/H}]_{\mathrm{m}}}$ adopt the values corresponding to the minimum uncertainties in the determination of the stellar parameters.

Another interesting test is to explore the effect of varying the size of the parametric cubes in which we start to find stars. We adopted in this Paper $1.5 \times \sigma_{p_0}$ but we list in the same table the values obtained for 0.5 1.0 and $3 \times \sigma_{p_0}$. A different, but related test, is to vary the applied enlargement to the size of these cubes when no stars are found after each iteration. The obtained residuals when adopting $1.5 \times \sigma_{p_0}$, rather than $0.5 \times \sigma_{p_0}$, are tabulated in Table C1. It is clear that the starting finding box size plays a more relevant role than the way in which the code expands this box when no stars are found. The largest residual, i.e. −0.12 Å, is found for [M/H] = −0.38 when adopting $0.5 \times \sigma_{p_0}$. However, for larger starting size values the obtained differences decrease.

Finally, we show the effect of adopting for $\sigma_{\theta_{\mathrm{M}}}$, $\sigma_{\log g_{\mathrm{M}}}$ and $\sigma_{[\mathrm{M/H}]_{\mathrm{M}}}$ several fractions of the total range covered by these parameters. Our reference value is $\frac{1}{10}$, but Table C1 lists the residuals when we set this limit to $\frac{1}{6}$, $\frac{1}{8}$ and $\frac{1}{12}$. By increasing this fraction we increase the weights assigned to the stars in the less populated regions of the parametrical space. This allow us to include stars for which the parameters are more distant from the requested point. The largest fractions (e.g. $\frac{1}{6}$) provides the largest effect on the Ca II triplet feature for the smallest and largest metallicities (i.e. [M/H] = −0.68 and = +0.2), where the CaT* weakens by 0.17 Å for [M/H] = −0.68 and strengthen by 0.06 Å for [M/H] = +0.2 with respect to our reference value. However, these differences become smaller as we approach our reference value, whilst for smaller fractions (e.g. $\frac{1}{12}$) the obtained differences are almost negligible for all metallicities. Overall we conclude that the SSP model predictions for the largest and smallest metallicities are subject to the largest uncertainties.

Table C1. Uncertainties of model calculation details on the CaT* index for SSPs of age 12.59 Gyr, unimodal IMF of slope 1.3 and different metallicities.

Test	Reference	Adopted	CaT*(adopted)−CaT*(reference) (Å)			
			[M/H] = −0.68	[M/H] = −0.38	[M/H] = 0.0	[M/H] = +0.20
T_{eff} where [M/H] is neglected	4000 K	3750 K	−0.080	0.059	0.046	0.052
T_{eff} where [M/H] is neglected	4000 K	4250 K	0.020	−0.005	−0.012	0.003
$\sum \rho_i(\rho_i < \rho_{\mathrm{M}})/\sum \rho_i$	99.7 per cent	100 per cent	−0.037	−0.020	0.000	0.006
$\sum \rho_i(\rho_i < \rho_{\mathrm{M}})/\sum \rho_i$	99.7 per cent	90 per cent	−0.012	0.015	0.028	0.008
Starting finding box size ($\times\sigma_{p_0}$)	1.5	0.5	−0.090	−0.118	0.000	0.016
Starting finding box size ($\times\sigma_{p_0}$)	1.5	1.0	−0.071	−0.020	0.000	0.001
Starting finding box size ($\times\sigma_{p_0}$)	1.5	3.0	−0.037	−0.047	0.009	0.033
Finding box size enlargement per iteration ($\times\sigma_{p_0}$)	0.5	1.5	−0.005	0.002	0.015	−0.021
p range fraction adopted for $\sigma_{p_{\mathrm{M}}}$	1/10	1/6	−0.166	0.002	0.016	0.059
p range fraction adopted for $\sigma_{p_{\mathrm{M}}}$	1/10	1/8	−0.083	−0.010	−0.008	0.030
p range fraction adopted for $\sigma_{p_{\mathrm{M}}}$	1/10	1/12	0.000	0.029	−0.003	−0.001

Table C2. The effect of the AGB on the CaT* for SSPs of different ages and metallicities. We use models of unimodal IMF of slope 1.3.

Age (Gyr)	ΔCaT*(AGB[no–yes]) (Å)			
	[M/H] = −0.68	[M/H] = −0.38	[M/H] = 0.0	[M/H] = +0.20
0.20			−0.499	
1.00			−0.087	0.157
3.16		0.000	0.185	0.120
10.00	0.000	−0.058	0.035	0.029

C2 Effects of varying the theoretical prescriptions of the stellar tracks

Here we focus on the effects caused by varying the theoretical prescriptions adopted for calculating the stellar evolutionary tracks and isochrones. We first discuss the effects derived from the most uncertain stellar evolutionary phase, i.e. the AGB. Then we discuss the effects of specific theoretical prescriptions affecting intermediate-aged stellar populations, such as the adopted convective overshooting scheme. Next, we focus on those prescriptions affecting old-aged stellar populations. Finally, we explore the effects of adopting stellar isochrones build up on the basis of non-solar element ratios.

We first show the effects of the AGB stellar evolutionary phase. We illustrate this study by means of performing a very crude approach, which is to remove this phase from the isochrones. Table C2 lists the obtained residuals for the CaT* index for SSPs of different ages and metallicities. For old stellar populations the effect of this evolutionary phase is very small, and the obtained residuals are of the order of the uncertainties derived in Appendix C1. As expected, the largest residuals, which can reach as high as ΔCaT*$\sim$0.5 Å, are obtained for ages below $\sim$1 Gyr. These residuals are significantly larger than those listed in Table C1. Obviously, this is a very crude test, which completely neglects our current knowledge of this late stellar evolutionary phase. In practice one expects to obtain smaller residuals owing to uncertainties in the AGB. This test shows us that the results presented in this paper for old stellar populations are stable against variations in the input physics of the most uncertain stellar evolutionary phase.

We plot in Fig. C1 the spectra obtained for an SSP of solar metallicity and 0.2 Gyr synthesized on the basis of including and excluding the whole AGB stellar evolutionary phase. We see that the overall shapes of these spectra are remarkably different. For these intermediate-aged SSPs the AGB stars are able to shape the continuum around the Ca II triplet feature in a way that is characteristic of M-type stars. Furthermore, without the AGB phase the Paschen lines clearly dominate the synthesized SSP spectra. This exercise also shows us to what extent it is important to work with an appropriate stellar spectral library, with a great coverage of the stellar atmospheric parameters including cool stars.

We have also explored the effects of varying other important theoretical prescriptions of the stellar evolutionary tracks, such as the adoption of a convective overshooting scheme. The new Padova isochrones (G00) have been updated on the basis of a significantly milder overshooting than that adopted for the old Padova isochrones (B94). Furthermore, G00 also provide a canonical set of solar metallicity isochrones, following the classical Schwarzschild criterion for the convective boundaries (i.e. without overshooting). The overshooting is only important for stellar masses greater than $\sim$1.2 $M_{\odot}$, therefore old-aged stellar populations are insensitive to the adopted scheme. We have transformed all of these isochrones to the observational plane following the same prescriptions described in Section 2.3. We then computed SSPs for different ages (i.e. from 0.2 to 10 Gyr) for solar metallicity and unimodal IMF (μ = 1.3). In Table C3 we list the obtained CaT* residuals. For SSPs of 0.2 and 1.0 Gyr the CaT* values provided by the canonical isochrones are larger than those based on the new Padova set, which are larger than those obtained from the old Padova isochrones. In fact, we obtain

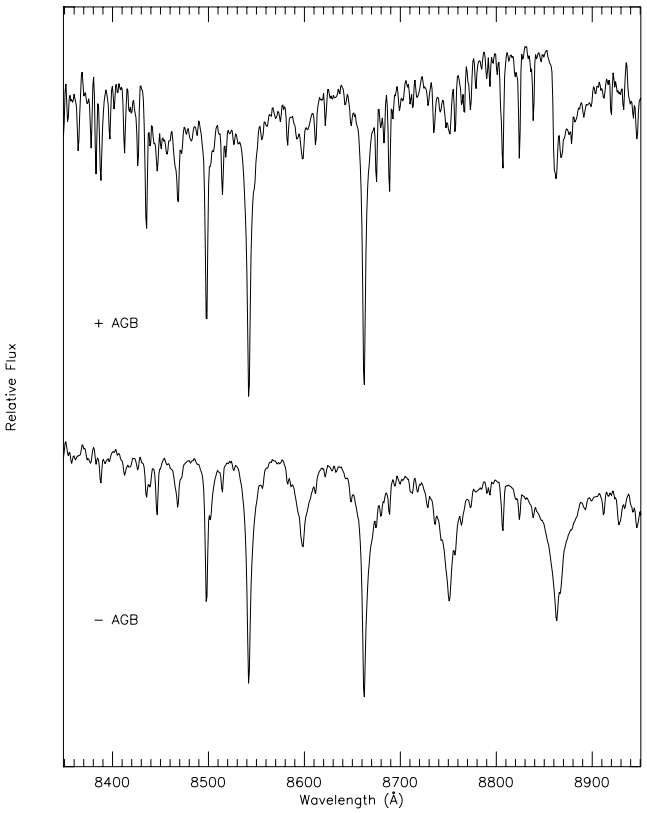

Figure C1. Synthetic SSP spectra for solar metallicity, 0.2 Gyr and unimodal IMF (μ = 1.3). For the upper spectrum we have included the AGB phase, whilst for the bottom spectrum we have excluded this stellar evolutionary phase. The spectral resolution is 1.5 Å (FWHM).

Table C3. CaT* index residuals owing to different theoretical prescriptions in the stellar evolutionary tracks. The obtained residuals are calculated for SSPs of different ages (indicated in gigayears), solar metallicity and unimodal IMF (μ = 1.3).

Age	ΔCaT*(Overshoot[no–yes])	ΔCaT*(Padova[old–new])
0.20	0.481	−0.600
1.00	0.826	−0.146
3.16	−0.016	−0.631
10.00	−0.003	−0.533

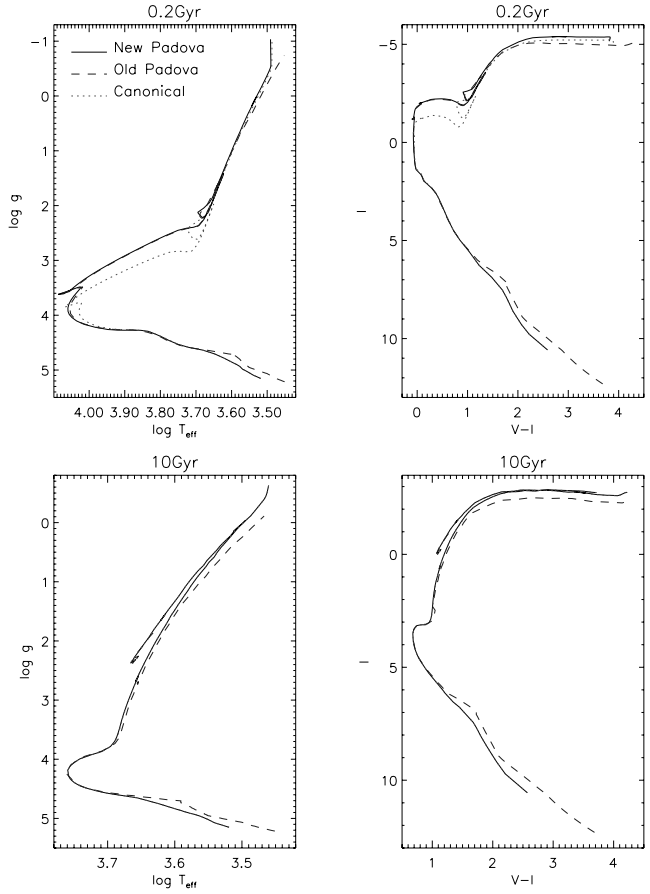

Figure C2. Plot of the new, old and canonical (i.e. without overshooting scheme) Padova isochrones for solar metallicity and 0.2 and 10 Gyr. See the text for details.

a total residual ΔCaT* $\sim$ 1 Å. As expected, no significant differences are found for old stellar populations owing to the adopted overshooting scheme (see the first column of residuals in Table C3), since stars with masses smaller than $\sim$1.1 $M_{\odot}$ present a radiative core during the MS. Fig. C2 shows the main differences between these three sets of isochrones for different ages.

For old-aged SSPs we find CaT* residuals larger than 0.5 Å when comparing the old and new Padova isochrones. The CaT* values provided by the old Padova set are smaller because they predict slightly cooler RGBs as shown in Fig. C2. For giant stars with temperatures smaller than $\sim$3500 K the Ca II triplet decreases with decreasing temperature (see Paper III). An exhaustive comparison of the theoretical parameters used to build up these two sets of isochrones is beyond the scope of this paper and we refer the interested reader to the G00 paper. However, it is worth recalling that if we replaced the model grids shown in Fig. 15 with those synthesized on the basis of the old Padova set of isochrones, which yield smaller CaT* strengths, we would derive smaller IMF slopes, i.e. $\Delta\mu \sim 1$ for the two galaxies plotted in this figure (see Section 8.2). Therefore, users of these SSP model predictions should be warned that, for this reason, IMF slope estimates must be taken into account on a relative basis. Despite the caveats, we believe that our predictions are still useful for obtaining robust conclusions, particularly when discussing possible trends among galaxies (see C03).

Elliptical galaxies show an enhancement of Mg over Fe when compared with scaled-solar SSPs model predictions (e.g. Peletier 1989; Worthey et al. 1992; V97; K00; V01A). Therefore, it is worth exploring the Ca II triplet strengths in SSPs synthesized on the basis of enhanced α-element mixtures. Such models require both stellar tracks calculated with appropriate opacity tables and stellar spectral libraries of similar α-enhanced ratios. However, no consensus has yet been reached for the degree of enhancement of different α-elements. For example, a constant enhancement for each α-element was adopted by VandenBerg et al. (2000) and Kim et al. (2002), whilst somewhat more empirically guided mixtures have been used by SW98 and S00. These authors find that, for a given total metallicity, the adoption of α-enhanced mixtures leads to higher effective temperatures with respect to scaled-solar for all evolutionary phases, and that, at relatively high metallicities and old ages, an α-enhanced isochrone cannot be mimicked by using a scaled-solar isochrone of different metallicity. It is worth noting that all of these stellar models adopt calcium-enhanced ratios as it is an α-element. However, the Ca 4227 line does not seem to track Mg but Fe in elliptical galaxies (V97; Trager et al. 2000a; T00; V01A; PS02). On the other hand, we do not expect any significant variation in the isochrone as a result of varying the degree of enhancement of this element, as its contribution to the total metallicity is lower than 0.5 per cent. The other important problem in synthesizing α-enhanced SSPs is the lack of stellar spectral libraries of appropriate α-enhanced mixtures. In particular, the empirical library used by our model follows the Galactic disc element ratios.

In spite of the fact that we are unable to build up such fully self-consistent α-enhanced SSP models for this spectral range, we are in a position to evaluate the isochrone effects on the synthesized spectra. For this purpose we have made use of both α-enhanced and scaled-solar isochrones of S00, which are constructed on the basis of almost the same input physics as that used in G00. Table C4 lists the residuals obtained for the CaT* index for SSPs of different ages and total metallicities. We find that the α-enhanced isochrones provide larger CaT* strengths for all the tabulated ages and metallicities. This is owing to the fact that the RGB of these isochrones is hotter and therefore there are a smaller number of stars falling into the cool temperature regime, where the strength of the CaT* decreases as a function of decreasing temperature (see Section 4.1 and Paper III for more details). We also see that the obtained residuals decrease as a function of increasing age. In particular, for old stellar populations of total metallicities [M/H] $\geqslant 0$ we obtain ΔCaT* ~ 0.5 Å, whilst for [M/H] $= -0.38$ we obtain ΔCaT* ~ 0.3 Å. Therefore, if we plotted these results in Fig. 15 we would obtain steeper IMF slopes for these two elliptical galaxies. Put in other way, if a Salpeter IMF is used, the α-enhanced isochrones lead to a larger calcium underabundance problem.

Table C4. CaT* residuals obtained for SSPs of different ages and metallicities (unimodal IMF of slope 1.3) calculated on the basis of the α-enhanced and scaled-solar isochrones of S00. We use a unimodal IMF ($\mu = 1.3$).

Age(Gyr)	ΔCaT*(α-enhanced – scaled-solar) (Å)		
	[M/H] $= -0.38$	[M/H] $= 0.0$	[M/H] $= +0.20$
0.20		0.954	
1.00		0.692	0.555
3.16	0.299	0.475	0.435
10.00	0.269	0.541	0.517

This paper has been typeset from a TEX/LATEX file prepared by the author.